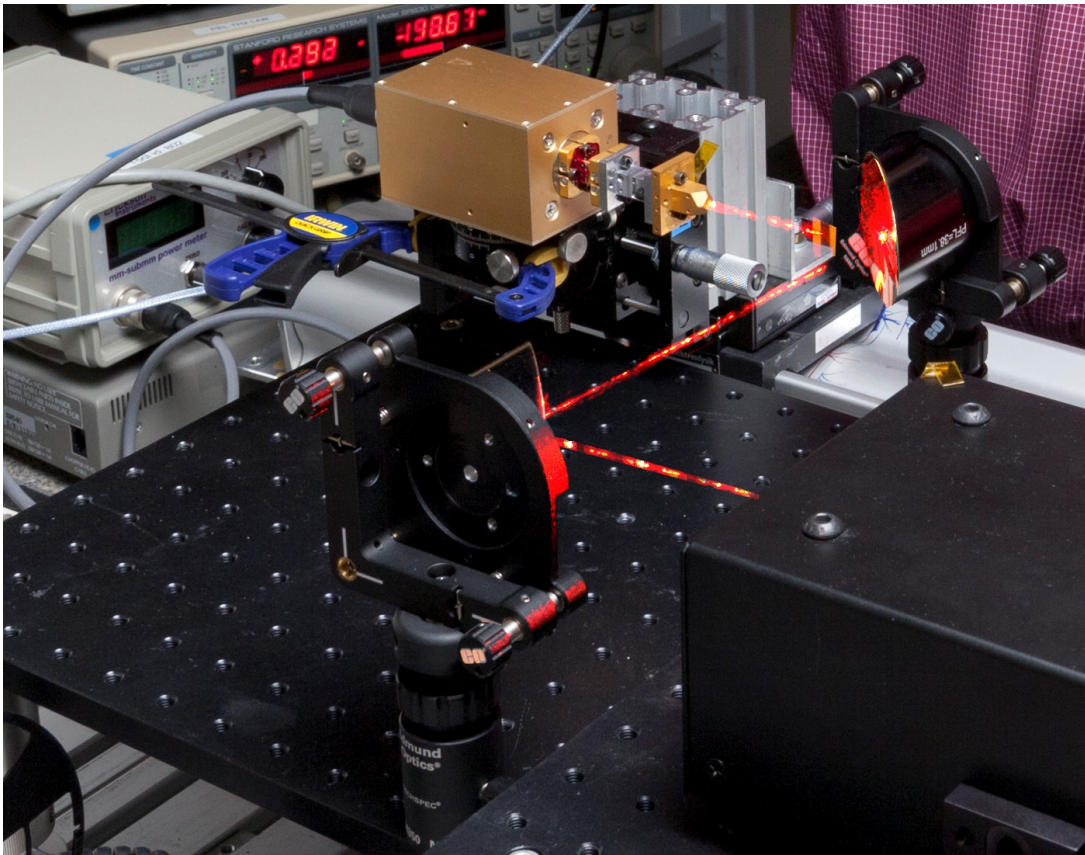


CHALMERS



Optical Simulations and Characterisations of Antenna Integrated YBCO THz Detectors

Master's Thesis in Wireless Photonics and Space Engineering

AUREL BERGFALK

Terahertz and Millimetre Wave Laboratory
Department of Microtechnology and Nanoscience - MC2
CHALMERS UNIVERSITY OF TECHNOLOGY
Göteborg, Sweden 2014

Master's Thesis in Wireless Photonics and Space Engineering

Optical Simulations and Characterisations of Antenna
Integrated YBCO THz Detectors

AUREL BERGFALK

Terahertz and Millimetre Wave Laboratory
Department of Microtechnology and Nanoscience - MC2
CHALMERS UNIVERSITY OF TECHNOLOGY
Göteborg, Sweden 2014

**Optical Simulations and Characterisations of Antenna Integrated YBCO
THz Detectors**
AUREL BERGFALK

© AUREL BERGFALK, 2014

Terahertz and Millimetre Wave Laboratory
Department of Microtechnology and Nanoscience - MC2
Chalmers University of Technology
SE-412 96 Göteborg
Sweden
Telephone + 46 (0)31-772 1000

Cover: Initial measurement on quasi-optical waveguide with Erikson PM2
Photo: Jan-Olof Yxell

This report is written in L^AT_EX

Göteborg, Sweden 2014

Optical simulations and characterisations of antenna integrated YBCO THz detectors

AUREL BERGFALK

Terahertz and Millimetre Wave Laboratory

Department of Microtechnology and Nanoscience - MC2

Chalmers University of Technology

Abstract

For accurate characterisation of quasi-optical terahertz (0.1 – 10 THz) detectors the beam pattern of both the detector and the transmitter antennas have to be optically matched. For this purpose a quasi-optical waveguide has to be designed to couple the RF power from the source antenna to the detector. This can be done using focusing elements such as lenses or mirrors. In this thesis the beam patterns from different hybrid antennas (planar antenna on a Si lens) are simulated using CST Microwave Studio and a quasi-optical waveguide with two parabolic mirrors is designed. It is shown that it is possible with standard desktop computers to simulate the whole hybrid antenna for frequencies in the lower terahertz region. It was discovered that a quasi-optical waveguide designed using parabolic mirror was more sensitive to misalignment than expected. The standing waves in the system were also more present than expected making the alignment even more difficult. The coupling loss through the diagonal horns and the quasi-optical waveguide relative to direct connection with WR-2.2 interface were measured to be 1.3 dB at 452 GHz and 1.5 dB at 389 GHz. Responsivity measurements on a YBCO bolometer with a log-spiral planar feed antenna mounted on a $\varnothing = 5$ mm lens were also performed. The measurements gave an optical responsivity of 30 V/w at 452 GHz and 40 V/w at 389 GHz. The bolometer used had an electrical responsivity of 50 V/w and was biased at 0.7 mA.

Keywords: ybco, bolometer, quasi-optical, terahertz, thz

Acknowledgments

First of all I would like to thank my supervisor Sergey Cherednichenko for giving me the opportunity to do this thesis and sharing some of his knowledge with me. I would also like to thank Robin Dahlbäck for assisting me in the use of the solver computer for the CST Microwave Studio simulations and Stella Bevilacqua for the assistance during the first bolometer measurements. Last but not least I would like to thank my wife for all the support and encouragement she has given me during the thesis work.

Aurel Bergfalk, Göteborg, March 3, 2014

List of Tables

3.1	Physical dimensions of the hybrid antenna M.J. van der Vorst at al pub.	14
3.2	CST MWS simulation duration for different frequency ranges.	15
3.3	Physical dimensions of the hybrid antenna Filipovic at al publication.	16
3.4	Physical dimensions of the hybrid antenna Jellema at al publication.	17
3.5	Contact pads' impact on the polarisation ellipse (without lens).	26
3.6	Contact pads' impact on the polarisation ellipse (with lens).	27
4.1	Beam waist radius for the horn and the hybrid antenna (from FWHM fit).	31
4.2	Beam waist radius for the horn and the hybrid antenna (from Gaussian fit).	32
4.3	Comparison between extracted beam waist sizes w diagonal horn.	35
4.4	Comparison between extracted beam waist sizes w hybrid antenna.	35
5.1	Design parameters for system with 2 parabolic mirrors 25 cm apart.	39
5.2	Design parameters for elliptical mirrors.	42
5.3	Parameters for two available 90° off-axis parabolic mirrors.	43
6.1	The maximum power levels measured with the mirrors in Z-configuration.	47
6.2	The maximum power levels measured with the mirrors in U-configuration.	49
6.3	Parameter values for responsivity measurements on the S6-6 device.	52

List of Figures

1.1	Illustration of the usually used method for calculating beam patterns. . .	2
2.1	Illustration on the principle of a bolometer.	4
2.2	Illustration of the hybrid antenna.	6
2.3	Illustration of the double-slot feed.	6
2.4	Illustration of the log-spiral feed.	7
2.5	Virginia Diodes WR-2.2 diagonal horn.	7
2.6	Beam parameters of a Gaussian beam.	8
2.7	The power distribution of a Gaussian beam.	9
2.8	Mirror off-axis reflection parameters.	11
2.9	Waist size or position misalignment effect on the coupling coeff. K_a	12
3.1	Far-field comparison with Van der Vorst et al paper.	15
3.2	Far-field comparison with Filipovic paper.	16
3.3	The dimensions of the hybrid antenna from Jellema et al publication. . .	17
3.4	SRON measurements comparison ellipse lens and slot antenna.	18
3.5	Figure of the lens and log-spiral feed from CST MWS simulations.	19
3.6	The far-field pattern of the hybrid antennas with the spiral feeds.	20
3.7	The far-field pattern of the VDI's WR-2.2 diagonal horn.	20
3.8	Nonphysical results from ADS MoM simulations at 2.5 THz.	22
3.9	Spiral antenna directivity comparison between simulations in CST MWS. . .	23
3.10	Spiral antenna directivity comparison between simulations in ADS MoM. . .	24
3.11	Contact pads' impact on the polarisation ellipse ADS MoM simulations. . .	25
3.12	Contact pads' impact on the polarisation ellipse CST MWS simulations. . .	26
3.13	The lens impact on the polarisation when simulated in CST MWS.	27
4.1	Simulated far-field patterns for diagonal horn and hybrid antennas.	30
4.2	Illustration of the 3 dB beam with	31
4.3	Gaussian fit for horn antenna.	33
4.4	Gaussian fit for hybrid antenna.	34

5.1	Gaussian beam propagation directly from antenna horn to hybrid antenna.	38
5.2	System set-up with two parabolic mirrors.	40
5.3	Gaussian beam with variation in system with two parabolic mirrors.	40
5.4	Elliptical reflector geometry parameters.	43
5.5	Parabolic mirrors dimension description.	44
6.1	Source-taper-sensor and source-horn-horn-sensor illustration.	46
6.2	The Z and U mirror configurations used for the measurements.	47
6.3	Measured power level with PM2 at different distances from mirror.	49
6.4	Figure of set-up with source horn mirrors and hybrid antenna.	50
6.5	Schematic view of the measuring set-up with bolometer and hybrid antenna.	50
6.6	Photo of the quasi-optical waveguide set-up.	51
6.7	Electrical responsivity extraction and the parallel diode impact.	51
6.8	The misaligned chip on the hybrid antenna.	54
A.1	Additional comparisons with the Van der Vorst et al. publication.	60
B.1	DC power versus resistance for the device S6-6.	61

Contents

Abstract	i
Acknowledgements	iii
List of tables	v
List of figures	v
Abbreviations and acronyms	xiii
1 Introduction	1
1.1 Background	1
1.2 Scope	1
1.3 Thesis outline	2
2 Theory	3
2.1 Bolometers	3
2.1.1 Bolometer responsivity	4
2.1.2 YBCO bolometers	5
2.2 Lenses with integrated planar feed	5
2.2.1 Double-slot antenna	6
2.2.2 Log-spiral feed	7
2.3 The diagonal horn	7
2.4 The Gaussian beam	8
2.5 Quasi-optical systems	9
2.5.1 Waist size or position misalignment	11
2.5.2 Mirror size and beam truncation	11
3 Antenna simulations	13
3.1 CST Microwave Studio	13
3.1.1 Validation of CST MWS simulations	14

3.1.2	Elliptical lens and double-slot feed	16
3.1.3	Elliptical lens and log-spiral feed	18
3.1.4	The diagonal horn	19
3.2	ADS momentum simulations	20
3.2.1	Problem with ADS MoM simulation	21
3.3	CST MWS and ADS MoM simulation comparison	21
3.3.1	Directivity comparison	22
3.3.2	The contact pads' impact on the polarisation	25
3.3.3	The lens impact on the polarisation	26
4	Parameter extraction	29
4.1	Gaussian fit of far-field patterns	29
4.1.1	Method 1: From the 3 dB beam width	29
4.1.2	Method 2: Using Gaussian fit with Matlab	31
4.1.3	Comparison results from different methods	32
4.2	The phase centre position	35
5	Measurement system implementation	37
5.1	Coupling between the antennas	37
5.2	Quasi-optical waveguide design	38
5.2.1	With two parabolic mirrors	38
5.2.2	Using one elliptical mirror	41
5.2.3	Edge taper of proposed systems	41
5.2.4	Choice of mirrors and configuration	41
6	Measurements and results	45
6.1	Measurement set-up	45
6.2	Initial calibration	46
6.2.1	Validation through waveguide taper	46
6.2.2	Directly horn to horn	46
6.2.3	Mirrors in Z-configuration	46
6.2.4	Mirrors in U-configuration	47
6.2.5	Standing waves	48
6.2.6	Difficulties with the alignment	48
6.2.7	Removing the taper	49
6.3	Bolometer measurements	49
6.3.1	Responsivity	52
6.3.2	Polarisation ellipse consideration	53
7	Discussion, conclusion and future outlook	55
7.1	The simulation part	55
7.2	Quasi-optical waveguide	56
7.3	Bolometer measurements	56
7.4	Future outlook	56

References	57
Appendix	59
A Additional far-fields comparisons	59
B Deterioration of bolometer	61
C VDI nominal horn specifications	63
D VDI waveguide band designations	65

Abbreviations and acronyms

ADS MoM	Agilent Advanced Design System momentum simulation tool
AR	Axial Ratio between orthogonal E-field components
CPU	Central Processing Unit
CST MWS	Computer Simulation Technology Microwave Studio
DSA	Double-Slot Antenna
EM	Electromagnetic
FWHM	Full Width at Half Maximum
LN ₂	Liquid nitrogen
MC2	Chalmers Department of Microtechnology and Nanoscience
MoM	Method of Moments
PM2	Erickson power meter PM2
RAM	Random Access Memory
RF	Radio Frequency
RFL	Reflected Focal Length
SRON	Space Research Organization Netherlands
TCR	Temperature Coefficient of Resistance
TML	Terahertz and Millimetre Wave Laboratory
YBCO	Ceramic compound YBa ₂ Cu ₃ O ₇ Yttrium Barium Copper Oxide

1

Introduction

THE TERAHERTZ REGION of the electromagnetic spectrum has long been used for spectroscopy and astronomical observations. In recent years interest in using it for medical and security applications has grown [1, 2]. The relative short wavelength makes it suitable for imaging in various medical applications since it still penetrates the body but without the harmful effects from ionizing radiations when using classical x-ray. The absorption of terahertz radiation in the atmosphere does not make it suitable for long way communication. For shorter distances it can be preferable due to the high available bandwidth and lack of noise from other distant transmitters [3].

1.1 Background

Chalmers MC2 has a history in making sensitive receivers for radio astronomy. Schottky diode, SIS (Superconductor Insulator Superconductor) junction, and bolometer based receivers have been successfully fabricated. Investigations have also been done on the high temperature super conducting ceramic compound $\text{YBa}_2\text{Cu}_3\text{O}_7$ Yttrium Barium Copper Oxide or short YBCO. Projects on this material have been carried out on Chalmers for some years. Earlier measurements and theoretical analyses have implicated that thin films of YBCO can have a large Temperature Coefficient of Resistance (TCR) even at room temperature [4]. New YBCO based bolometer detectors are now developed at the Terahertz and Millimetre Wave Laboratory at Chalmers MC2. These devices have to be characterised to determine their performance.

1.2 Scope

For accurate characterisation of quasi-optical terahertz (0.1–10 THz) detectors the beam pattern of both the detector and the transmitter antennas have to be optically matched. For this purpose a quasi-optical waveguide has to be designed that efficiently couples

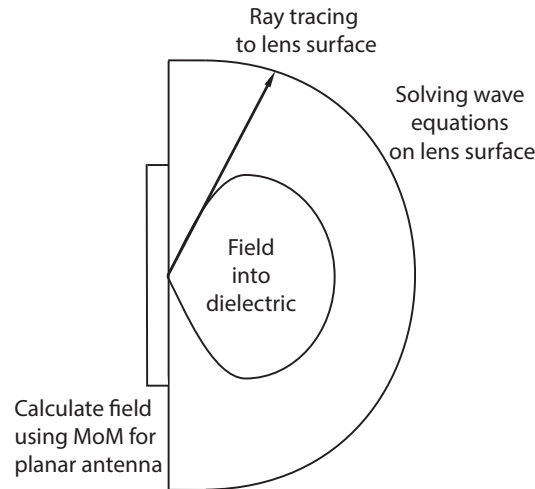


Figure 1.1: Illustration of the usually used method for calculating beam patterns for lens antennas with integrated planar feeds.

the RF power from the source antenna to the detector. This is what will be done in this thesis. To design optically matched quasi-optical waveguide the beam patterns of the transmitter antenna end receiver antenna have to be known. Usually antennas used for the bolometer receivers (lenses with integrated planar feeds) are simulated in several steps. First a beam pattern of the planar feed is simulated. The result is then used to calculate how the beam will look after the air lens interface with some beam tracing software. See figure 1.1. In this thesis project, the lens and radiating planar feed will be simulated together using CST Microwave Studio transient solver. This puts a high demand on the computing power and memory usage of the computer. The simulation results will be used to design a quasi-optic waveguide to couple the radiation from a transmitter horn to the integrated lens antenna. This quasi-optical waveguide can then be used to investigate the performance of the fabricated bolometers when integrated with the antenna and lens. Computer simulations are only performed on already fabricated devices so no new antennas will be designed and optimised.

1.3 Thesis outline

Chapter 2 describes the basic theory used for calculations in the thesis. In chapter 3 the antenna simulations are described and the beam patterns of the antennas are presented. In chapter 4 the Gaussian beam parameters are extracted from the simulations with two different methods. In chapter 5 the simulation results are used to design the quasi-optical waveguide. In chapter 6, the simulations and the quasi-optical waveguide design are validated with measurements and the final results are presented. Chapter 7 contains an overall discussion and conclusion of the thesis and future works are proposed.

2

Theory

The chapter starts with an introduction to the bolometer and the basic concept of its functionality. This is followed by a basic description of the receiver and transmitter antennas used in the thesis. The last part of the chapter deals with the basic Gaussian beam approximation theory.

2.1 Bolometers

The bolometer was invented 1878 by Samuel P. Langley [5]. The basic principle of a bolometer is that the absorption of the incident radiation increases the temperature of the device. This increase in temperature is then measured. An illustration of the bolometer principle can be found in figure 2.1. The absorber must have high absorptivity for the desired radiation. Despite the long history of the bolometer it was not until the latter half of the 20th century it started to be more frequently used as a detector [6]. As for all thermal radiation detectors the bolometers speed is characterised by a time constant τ .

$$\tau = \frac{C}{G} \tag{2.1}$$

C is the heat capacity of the absorber and G is the thermal conductance between the absorber and the heat sink, see figure 2.1. There is a trade-off between the bolometer sensitivity and the speed. The bolometers sensitivity is proportional to $\frac{1}{G}$. To keep the time constant from equation (2.1) small C must also be reduced. The heat capacity C is related to the volume V of the device according to $C = C_V \cdot V$ in which C_V is the volumetric heat capacity. This motivates the use of nanobolometers.

When power is absorbed the temperature T_B of the absorber increases initially with time rate of $\frac{dT_B}{dt} = \frac{P}{C}$ until the power is turned off or the limit $T_B = T_S + \frac{P}{G}$ is reached. When no power is absorbed the temperature of the absorber relaxes back to T_s . The relaxation time or response time is τ .

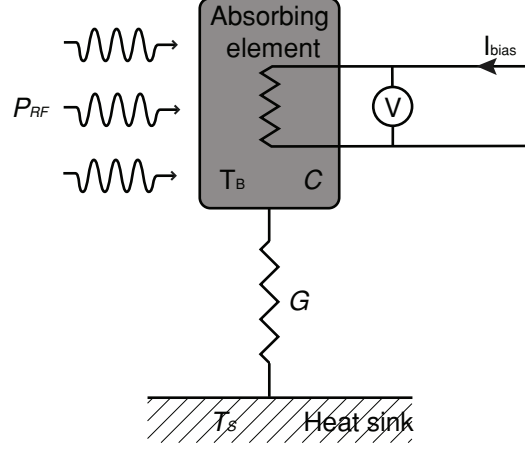


Figure 2.1: Illustration of the bolometer principle. C is the heat capacity of the absorber and G is the thermal conductance between the absorber and the heat sink. T_B and T_S is the temperature of the bolometer absorber and heat sink respectively.

2.1.1 Bolometer responsivity

When the bolometers are used as direct detectors and the modulation frequency, time constant relation $\omega \ll \frac{1}{\tau}$ is fulfilled, the bolometers voltage responsivity relative to an amplitude modulated RF signal can be obtained from the following two thermal balance equations [4]:

$$G \cdot (T_B - T_S)_{\text{RF,off}} = I_{\text{bias}}^2 \cdot R_{\text{RF,off}} \quad (2.2)$$

$$G \cdot (T_B - T_S)_{\text{RF,on}} = I_{\text{bias}}^2 \cdot R_{\text{RF,on}} + P_{\text{RF}} \quad (2.3)$$

$R_{\text{RF,off}}$ is the resistance of the absorbing element when no P_{RF} is absorbed and $R_{\text{RF,on}}$ is the resistance of the absorbing element when P_{RF} is absorbed. Other parameters used in the equation can be found in figure 2.1. The bolometers used here are nanobolometers made of YBCO on a sapphire (Al_2O_3) substrate. The absorbing element is a small strip of the YBCO film in the centre of an antenna and the heat sink is the substrate. The bolometer is biased with some milliamperes I_{bias} that heats the bolometer T_B above the substrate temperature T_S and then the change in temperature $(T_B - T_S)_{\text{RF,off}}$ can be seen in the change of the resistance $R_{\text{RF,off}}$ of the device. When the RF power is turned on, the absorbed RF power P_{RF} will increase the temperature T_B making the difference $(T_B - T_S)_{\text{RF,on}}$ larger and the absorber will get a new resistance $R_{\text{RF,on}}$. The index (RF on/off) indicates if RF power P_{RF} is on or off (absorbed or not absorbed). The parameter needed in this thesis for the characterisation of the bolometers is the optical responsivity of the bolometer. The optical responsivity is defined as the change in voltage for a given absorbed RF power $R_V = \frac{\Delta U}{\Delta P}$. The bolometer is assumed to be biased with a constant

current I_{bias} . Combining equation (2.2) and (2.3) and extracting $\frac{\Delta U}{\Delta P}$ we get

$$\frac{\Delta U}{\Delta P} = \frac{I_{\text{bias}} \left(\frac{\partial R}{\partial T} \right)}{G - I_{\text{bias}}^2 \left(\frac{\partial R}{\partial T} \right)} \quad (2.4)$$

The TCR is defined as $\alpha = \left(\frac{\partial R}{\partial T} \right) \frac{1}{R}$. Using this in equation (2.4) we get

$$R_V = \frac{I_{\text{bias}} \cdot \alpha \cdot R}{G - I_{\text{bias}}^2 \cdot \alpha \cdot R} \quad (2.5)$$

2.1.2 YBCO bolometers

In 1986 Georg Bednorz and Karl Müller, working at IBM in Zurich, discovered that some semiconducting oxides become superconducting at relatively high temperatures around 35 K. Later in 1987 YBCO (Yttrium Barium Copper Oxide) was discovered [7]. Since the critical temperature of YBCO is above 77 K, liquid nitrogen LN₂ can be used as coolant to reach the superconducting state. However as was mentioned in the introduction measurements made in this thesis will only be done at room temperature.

2.2 Lenses with integrated planar feed

Due to the bolometers small dimension ($\lambda \gg A$, A -bolometer area) an antenna is needed to efficiently couple the RF radiation to the bolometer, but the wavelength of terahertz radiation (30 μm – 3000 μm) makes the antenna dimensions really small. The small dimensions of the antennas make them suitable for integration with the bolometer directly on the substrate wafer. With this method radiation loss to substrate modes arises if the substrate is thicker than some fraction of the wavelength ($0.02\lambda_0$) [8]. For these short wavelengths the substrate have to be very thin making them very fragile. One way of coupling the energy to the antenna but still using thicker substrate is by attaching the substrate to the back of a dielectric lens with the same permittivity as the substrate. The lens couples the radiation to or from the feed in a desired direction with no substrate modes. High resistivity silicon lenses is often used since they have similar dielectric constant as the substrates. The dielectric constant of silicon is $\epsilon_r \approx 11.7$. The sapphire used in the substrate is a uniaxial birefringent material so the dielectric constant depends on the incident angle of the radiation $\epsilon_r \approx 9.5 - 11.5$ [9]. The high permittivity forces most of the radiation from the planar antenna to be coupled through the lens and substrate. The ratio of power coupled to the dielectric instead of air is $\epsilon_r^{3/2}$ for a double-slot antenna [8]. An illustration of a lens with integrated planar feed can be found in figure 2.2. With this technique a high number of bolometers with planar feed antennas can easily be installed on the same lens making up an array that can be used for imaging. A lens with an integrated planar feed will in this thesis be referred to as a hybrid antenna. The hybrid antenna feeds used in this thesis are double-slot feed for validation simulations and a log-spiral feed for final simulations and measurements.

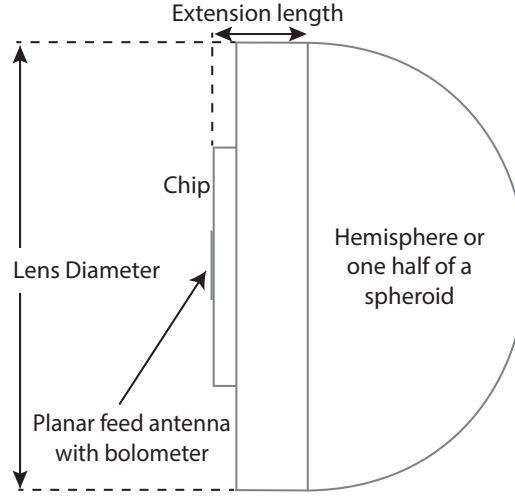


Figure 2.2: Illustration of the hybrid antennas used in this project. To the left is the substrate chip with the integrated antenna on the left most surface.

2.2.1 Double-slot antenna

A layout of a planar Double-Slot Antenna (DSA) can be seen in figure 2.3. The dimensions for a feed antenna used with a silicon lens are usually $L \approx 0.30\lambda_0$, $S \approx 0.16\lambda_0$ and $W \approx 0.05\lambda_0$ [8, 10]. The dimensions a and b have a minor impact on the boresight field pattern, they are often used to tune the impedance of the antenna.

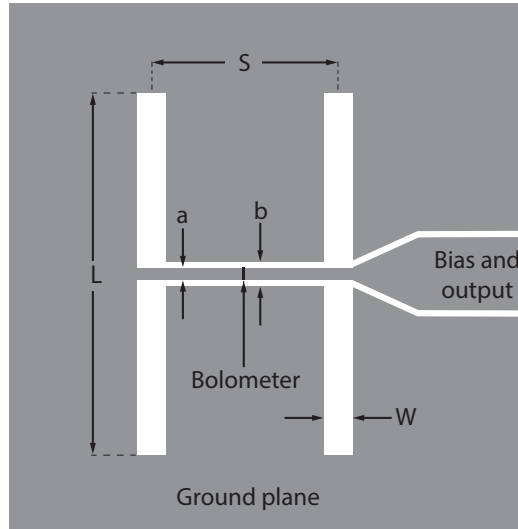


Figure 2.3: Illustration of a double-slot feed. The contacts on the right were never included during simulations. L is the slot length, W is the slot width and S is the slot separation. The dimensions a and b are usually not specified.

2.2.2 Log-spiral feed

Spiral antennas are used because of their large bandwidth and that the real part of the impedance are relative constant for a wide frequency range. In theory a spiral antenna can have infinite bandwidth but its physical size sets the limits. A rule of thumb for log-spiral feeds used on silicon are that $\lambda_{\min} \approx 20 \mathbf{d}$ and $\lambda_{\max} \approx 6 \mathbf{D}$ [10].

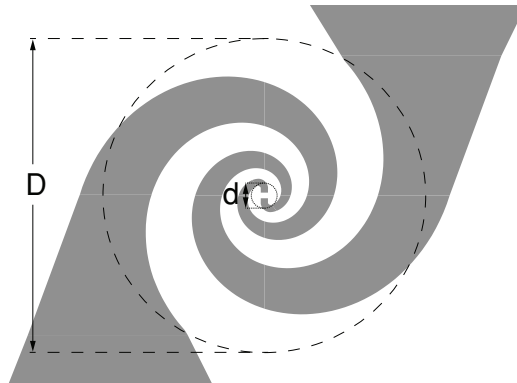


Figure 2.4: Illustration of a log-spiral feed. The size \mathbf{D} sets the lower limit and \mathbf{d} sets the upper limit of the frequency.

2.3 The diagonal horn

The source feed will be a WR-2.2 diagonal horn from Virginia Diodes (VDI) [11]. The diagonal horns are multi-mode horns. The resulting field is the superposition of the TE_{10} and the TE_{01} mode [12]. Specifications for the different horn types from VDI can be found in appendix C.

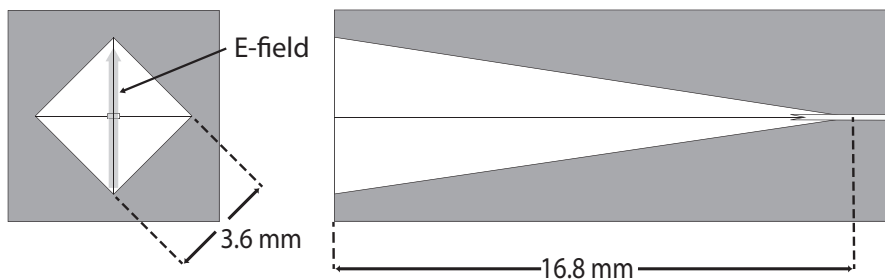


Figure 2.5: The Virginia Diodes diagonal horn with a WR-2.2 waveguide connection, used in simulations and later in measurements.

2.4 The Gaussian beam

The radiation field from a horn or a hybrid antenna can be approximated as a Gaussian beam. Only the fundamental mode is used in this thesis (multi-modal Gaussian design can be used for more precise calculations). If a cylindrical coordinate system is aligned so the boresight of the radiation beam is located along the z -axis, then equation (2.6) describes the normalised transverse field distribution at an orthogonal plane, at the distance z away from the beam waist $w(z=0) = w_0$ [13].

$$E(r,z) = \sqrt{\frac{2}{\pi w^2(z)}} \exp \left[\frac{-r^2}{w^2(z)} - jkz - \frac{j\pi r^2}{\lambda R(z)} + j\phi_0(z) \right] \quad (2.6)$$

A description of the Gaussian beam and its parameters can be found in figure 2.6.

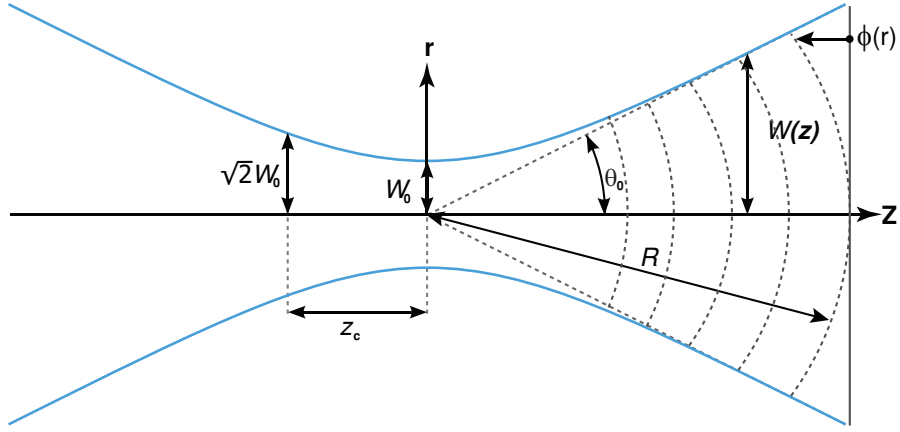


Figure 2.6: The beam, waist radius w_0 , radius $w(z)$, radius of curvature R , divergence angle θ_0 , phase delay $\phi(z)$ and the confocal distance z_c , of a Gaussian beam in a cylindrical coordinate system.

To solve equation (2.6) the following parameters are needed. Wavelength λ , beam radius $w(z)$, radius of curvature $R(z)$ and the Phase shift $\phi_0(z)$ on a plane orthogonal to the boresight direction and at a distance z . These parameters are given by equation (2.7) – (2.9) in which z_c is the confocal distance which is given by equation (2.10). The beam radius $w(z)$ is defined as the distance from boresight (z -axis) to the point away from the z -axis where the electrical field has dropped $E = \frac{E_{r=0}}{e}$ below the maximum value (boresight $r = 0$). See figure 2.7.

$$w(z) = w_0 \sqrt{1 + \left(\frac{z}{z_c} \right)^2} \quad (2.7)$$

$$R(z) = z + \frac{z_c^2}{z} \quad (2.8)$$

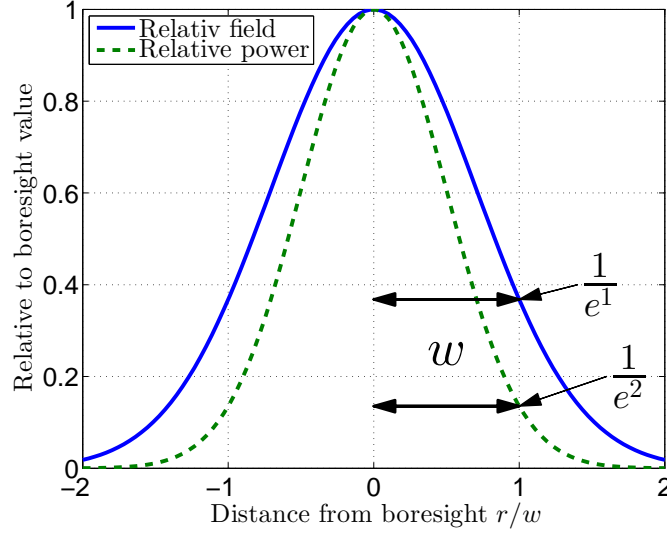


Figure 2.7: The power distribution of a Gaussian beam and the position of the beam radius defined as the distance from boresight where the electrical field has dropped to $E(r) = E(0)/e$ or equivalent the power level is has dropped to $P(r) = P(0)/e^2$.

$$\phi_0(z) = \arctan\left(\frac{z}{z_c}\right) \quad (2.9)$$

$$z_c = \frac{\pi w_0^2}{\lambda} \quad (2.10)$$

If the wavelength λ and beam waist radius w_0 are known, the transverse field distribution of a Gaussian beam can be calculated at any plane at a distance z away from the direction of propagation. The far-field of a Gaussian beam is defined as distances z beyond ($z \gg z_c$). Equation 2.8 gives that $R(z \gg z_c) \approx z$ as seen in figure 2.6. The far-field divergence angle θ_0 is calculated with equation (2.11).

$$\theta_0 = \lim_{z \gg z_c} \left[\arctan\left(\frac{w}{z}\right) \right] = \arctan\left(\frac{\lambda}{\pi w_0}\right) \quad (2.11)$$

2.5 Quasi-optical systems

Lenses and mirrors are focusing elements that can be used to transform Gaussian beams. If the thin lens approximation is used the relation between the input $w_{0,\text{in}}$ and output $w_{0,\text{out}}$ beam waist of a focusing element is given by equation (2.12). d_{in} is the distance between the focusing element and the input waist $w_{0,\text{in}}$. The source of the input waist $w_{0,\text{in}}$ has a confocal distance z_c . f is the focal length of the focusing element (mirror or

lens).

$$w_{0\text{ out}} = \frac{w_{0\text{ in}}}{\sqrt{\left(\frac{d_{\text{in}}}{f} - 1\right)^2 + \frac{z_c^2}{f^2}}} \quad (2.12)$$

When mirrors or lenses are used to transform a beam waist $w_{0,\text{in}}$ to a new beam with a beam waist $w_{0,\text{out}}$ the system is said to have a magnification defined by equation 2.13.

$$\mathfrak{M} = \frac{w_{0,\text{out}}}{w_{0,\text{in}}} \quad (2.13)$$

Equation (2.12) gives that the maximum magnification $\mathfrak{M}_{\text{max}}$ for a given optical element occurs when the input waist is at the focal point $d_{\text{in}} = f$, giving $\mathfrak{M}_{\text{max}} = f/z_c$.

Both lenses and mirrors introduce distortions and losses. Lenses introduce absorptive and reflective losses in a greater extent than mirrors and mirrors have better power handing capabilities and are thereby a more attractive choice for use as refocusing elements [13]. Even if the mirrors would have perfect reflective surface some of the power from the fundamental mode would still be lost, since the mirrors have to be used in off-axis configurations to avoid beam blockage. The off-axis configuration contribute with losses due to amplitude and phase mismatch at the mirror surface and the loss is given by equation (2.14). Losses also occur since some of the radiation change polarisation and become cross-polarised. The power loss from polarisation change can be calculated with equation (2.15) [14]. w_m is the beam width at the mirror, f is the nominal focal length of the mirror and θ_i is the angle of the incident and the reflected beam relative to the normal of the lens. Se figure 2.8.

$$\Delta P_f = \left(\frac{w_m}{2\sqrt{2}f}\right)^2 \tan^2 \theta_i \quad (2.14)$$

$$\Delta P_{\text{co}} = \left(\frac{w_m}{2f}\right)^2 \tan^2 \theta_i \quad (2.15)$$

If multiple mirrors are used the loss are accumulated as in equation (2.16) in which $\Delta\phi_{k \rightarrow k+1}$ is the phase slippage of the fundamental mode between mirror k and $k+1$. For losses from phase and amplitude mismatch, $\alpha = 3$ and $\beta = \frac{1}{2\sqrt{2}}$. For losses due to cross-polarisation shift, $\alpha = 1$ and $\beta = \frac{1}{2}$.

$$\Delta P = \left| \sum_{j=1}^n \left[\beta \left(\frac{w_m}{f}\right)_j \tan(\theta_{i,j}) \exp\left(-j \sum_{k=1}^n \alpha \Delta\phi_{k \rightarrow k+1}\right) \right] \right|^2 \quad (2.16)$$

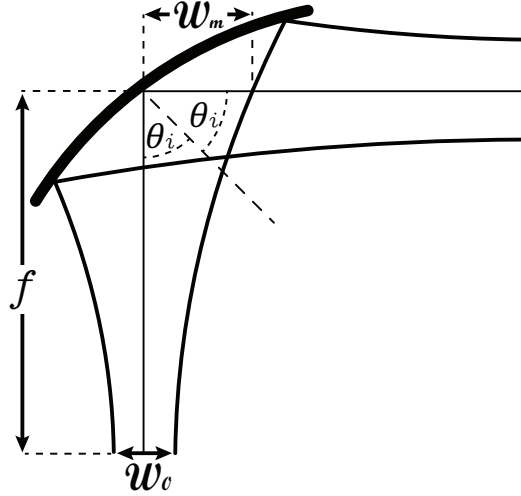


Figure 2.8: Parameters needed for calculating the off-axis reflection loss introduced by a mirror.

2.5.1 Waist size or position misalignment

If the polarisation effects are neglected the power coupling coefficient K_a for imperfectly coupled beams with axial alignment can be calculated with equation (2.17), [13].

$$K_a = \frac{4}{\left(\frac{w_{0b}}{w_{0a}} + \frac{w_{0a}}{w_{0b}}\right)^2 + \left(\frac{\lambda\Delta z}{\pi w_{0a}w_{0b}}\right)^2} \quad (2.17)$$

Δz is the misalignment distance of the beam waists w_{0a} and w_{0b} . Figure 2.9(a) shows the effect on the coupling coefficient when the beam waists positions are aligned but the beam waist sizes do not match. Figure 2.9(b) shows the effect on the coupling coefficient when the beam waist sizes match but the beam waist positions are misaligned along the axis of propagation.

2.5.2 Mirror size and beam truncation

One parameter not considered in the calculations above is the diameter of the mirrors, required for good coupling of the Gaussian beam. Since the fundamental mode only is considered, the field strength decays with a rate of $1/e$ when moving away from the axis of propagation (figure 2.7). A finite size of the mirrors will truncate the beam, resulting in a broadening of the main beam and diffraction [13, 15]. The broadening of the beam has the same effect as if having a beam with a smaller beam waist than the original beam. This new beam waist is referred to as the effective beam waist $w_{0,\text{eff}}$. If a truncation of the beam is placed at the waist w_0 of the beam the effective beam waist $w_{0,\text{eff}}$ can be calculated with equation (2.18)

$$\frac{w_{0,\text{eff}}}{w_0} = 1 - \sqrt{T_e} \quad (2.18)$$

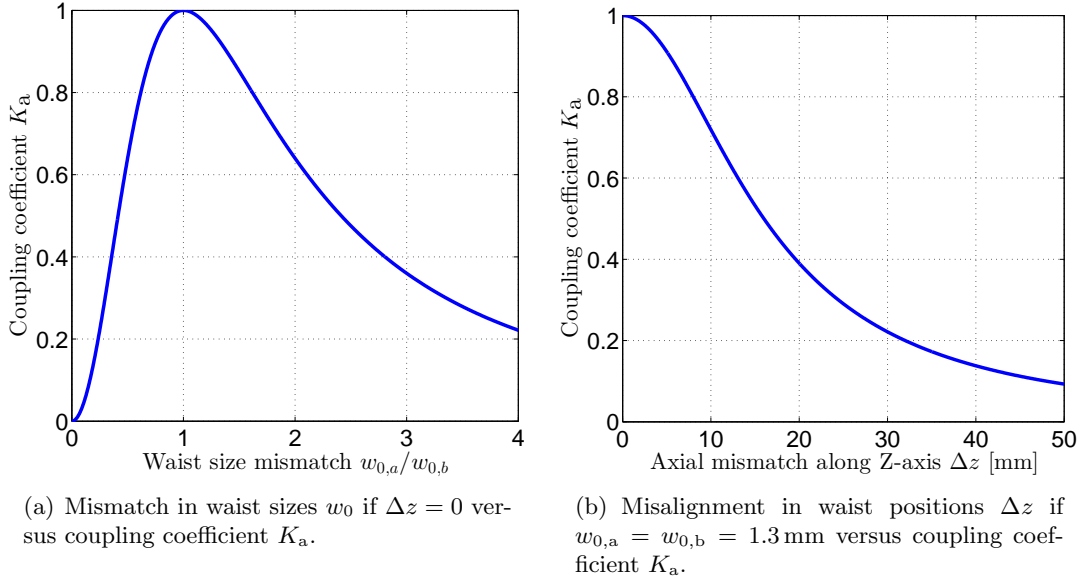


Figure 2.9: Effect on the coupling coefficient K_a when the waist size or waist position along axis of propagation do not match.

T_e is the edge taper and corresponds to the relative power level at a radius r_e from the axis of propagation. The edge taper is usually expressed in decibel according to equation (2.19). In the case of a mirror, r_e corresponds to the radius of the mirror.

$$T_e(\text{dB}) = -10 \log_{10} \left[\exp \left(\frac{-2r_e^2}{w^2} \right) \right] \quad (2.19)$$

For equation (2.18) to be valid the edge taper of $T_e \geq 20$ dB is required. When the truncation is situated in another location than the beam waist the situation becomes more complex. Usually when a higher number of mirrors are used and some are placed in the near field of a beam waist a simple approach successfully used by many designers for systems with a few mirrors is $D_{\min} = 4w$ [13]. A mirror diameter of $4w$ gives an edge taper of 34.7 dB. An edge taper of 34.7 dB corresponds to a power loss of only 0.04% and a 2% smaller waist if the mirror is placed at the beam waist location.

3

Antenna simulations

The chapter starts with a description and validation of the CST MWS simulations. The second section deals with the Agilent ADS momentum simulations. Last in the chapter results from the different simulations are compared and the antenna contact pads effect on the simulations are discussed.

3.1 CST Microwave Studio

CST Microwave Studio is a 3D EM simulation software included in the CST Studio Suite developed by CST - Computer Simulation Technology [16]. In this thesis the time domain transient solver in CST Microwave Studio (CST MWS), based on the Finite Integration Technique (FIT) were used for the major part of the simulations. When simulations like these are performed there is always a trade-off between accuracy and computing time. The available computing power and available RAM memory set a limit on what is possible to simulate to a certain accuracy. Most of the CST simulations during this thesis work were done on a special solver computer with 2 Intel Xeon E5640 CPUs running at 2.67 GHz and 96 GB of RAM. One important setting when simulating with CST MWS is the mesh density setting. The object to be simulated is divided into mesh cells. This can be done automatically in CST MWS by just setting the minimum desired number of mesh lines in each coordinate needed for the simulation. The number of lines is set in lines per wavelength according to the highest simulation wavelength. The program manufacture recommends a setting of 10 lines per wavelength. The shortest distance between two mesh lines is also an important setting. This decides the time step used during the simulation and has a large influence on the simulation time. The shortest distance has to be smaller or equal to the smallest dimension of the simulated structure. When the simulation is started the field equations are solved for each mesh cell and time step. The calculations continues for a selected number of time steps or until a desired accuracy value is reached. To get fast and accurate simulations in CST

transient solver it is decided to use wide frequency range but not so wide that it contains resonating frequencies.

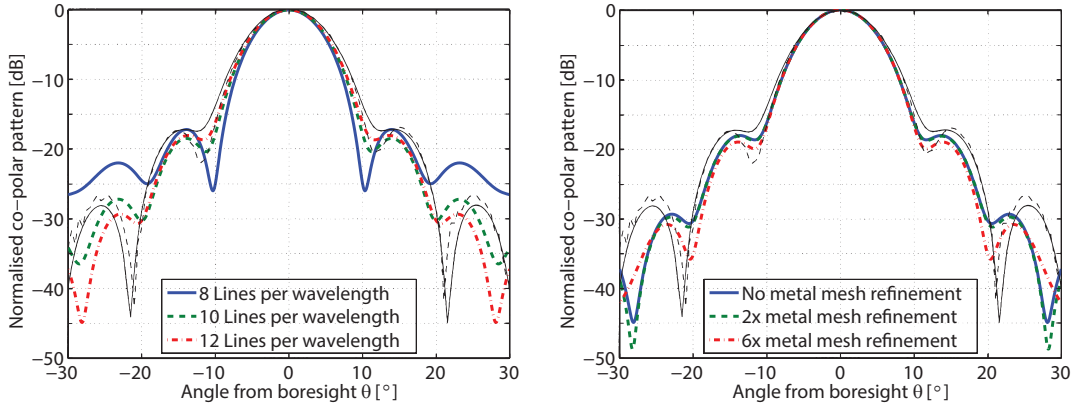
3.1.1 Validation of CST MWS simulations

To investigate if the simulated beam patterns are consistent with measured beam patterns, hybrid antennas from other publications were simulated and then the results were compared with measurement results from the publications. The majority of all published simulations with hybrid antennas are done with a double-slot antenna as a radiating source. In most cases it is not possible to get details on the measurement set-up and other conditions such as antenna chip size, slot width and bias connection appearance. This makes it impossible to get a real accurate comparison without self performing the measurements under desired conditions. A publication by M.J. van der Vorst et al [17] is fairly detailed on the conditions and specifications during measurements on a hemispherical lens and slot antenna. The published physical parameters of the hybrid antenna used for the measurements in the paper can be found in table 3.1. This publication was first used for comparison to decide which CST MWS simulation settings to use during the rest of the simulations. In figure 3.1 simulation results are

Table 3.1: Physical dimensions of the hybrid antenna and in which figure they are represented. These dimensions were used in the comparison with the M.J. van der Vorst et al publication [17].

Dimension name	parameter	value	Figure reference
Lens diameter	\varnothing	4 mm	2.2
Lens extension length	l	670 μm	2.2
Slot length	L	168 μm	2.3
Slot separation	S	93 μm	2.3
Slot width	W	8 μm	2.3

plotted on top of the figures from the publication for easy comparison. There is a major difference in the H-plane far-field co-polar pattern in results from simulations with 8 and 10 lines per wavelength as seen in figure 3.1(a). The difference between 10 and 12 lines per wavelength is less. There is a setting for mesh refinement at the metal edges. With this setting the program can use a finer mesh at the metal edges to get a more accurate result for the fringe fields. The setting is activated by entering how many times finer the mesh should be at the metal edges. Far-field comparison between simulations with 12 lines per wavelength in global setting and no mesh refinement, 2 times refinement and 6 times refinement can be found in figure 3.1(b). The effect of refining the mesh at the metal edges appears to have a greater impact at the side-lobes than on the main-lobe. With 12 lines per wavelength and 6 times metal edge refinement setting simulations for different frequency ranges were done on the device from table 3.1. The simulation time



(a) The far-field simulated with CST MWS using different lines per wavelength settings with no metal edge mesh refinement.

(b) The far-field simulated with 12 lines per wavelength in CST MWS using different metal edge mesh refinement settings.

Figure 3.1: The far-field in the H-plane calculated with CST MWS at 497 GHz for a $\varnothing = 4$ mm lens with a $670 \mu\text{m}$ extension and anti-reflection coating. The black thin lines are the simulated (—) and measured (- -) results from the publication [17].

for different frequency ranges can be found in table 3.2. All the simulations in table 3.2 gave the same far-field pattern at 497 GHz.

Table 3.2: CST MWS simulation duration for different frequency ranges. All giving the same far-field pattern at 497 GHz.

Frequency range [GHz]	Simulation duration [h:m:s]
100-600	7:21:41
400-600	4:06:31
450-600	3:39:33
490-600	3:45:37

Additional comparisons with the Van der Vorst et al. publication can be found in appendix A.

Hybrid antennas simulated and measured by Filipovic et al. [8] are also simulated with CST MWS and the results compared. The exact dimensions of the double-slot feed are not specified in the publication, but they were calculated according to the specifications given in the publication for a frequency of 246 GHz giving $\lambda_{\text{air}} \approx 1.2$ mm. The specifications can be found in table 3.3. The simulations with data from Filipovic publication were in fairly good agreement for the $2700 \mu\text{m}$ extension on a $\varnothing = 13.7$ mm extended hemispherical lens as seen in figure 3.2(a). The beam pattern for a hemispherical lens with $2200 \mu\text{m}$ extension was not as consistent (figure 3.2(b)). The reason for

Table 3.3: Physical dimensions of the hybrid antenna and in which figure they are represented. These dimensions were used in the comparison with the Filipovic at al publication [8].

Dimension name	parameter	value	Figure reference
Lens diameter	\varnothing	13.7 mm	2.2
Lens extension length	l	2700 μm and 2200 μm	2.2
Slot length	L	$0.28\lambda_{\text{air}} \approx 342 \mu\text{m}$	2.3
Slot separation	S	$0.16\lambda_{\text{air}} \approx 195 \mu\text{m}$	2.3
Slot width	W	30 μm	2.3

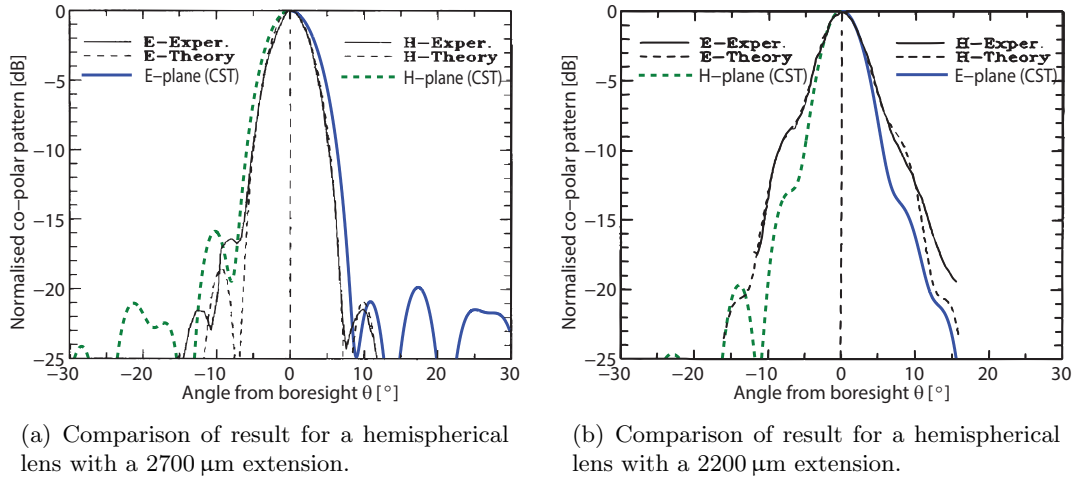


Figure 3.2: Comparison between CST MWS simulation results (solid blue) E-plane, (dashed green) H-plane and simulated and measured results from publication [8].

this is not clearly investigated. One source of error is the fact that the exact design of the antenna such as size of ground plane and slot width used during measurements and the exact set-up used are hard to replicate since they are not specified in detail in the published paper. The slot width of 30 μm was estimated from by measuring with a ruler in a figure of the antenna.

3.1.2 Elliptical lens and double-slot feed

A beam pattern of a DSA with a $\varnothing = 5 \text{ mm}$ elliptical lens has been simulated and measured by Jellema et al. at the Space Research Organization Netherlands, SRON [18]. This lens dimensions were used in the design of the quasi-optical waveguide. In the publication they used a double-slot feed with the dimension described in table 3.4. The set-up of the hemispherical lenses used in earlier simulations were easy and straight forward. In this case the lens is elliptical so the sphere and cylinder tools in CST MWS

Table 3.4: Physical dimensions of the hybrid antenna and in which figure they are represented. These dimensions were used in the comparison with the Jellema et al publication [18].

Dimension name	parameter	value	Figure reference
Lens diameter	\varnothing	5 mm	3.3(b)
Semi-major axis	a	2.548 mm	3.3(b)
Semi-minor axis	b	2.5 mm	3.3(b)
Lens extension length	l	756 μm	3.3(b)
Slot length	L	56 μm	3.3(a)
Slot separation	S	32 μm	3.3(a)
Slot width	W	4 μm	3.3(a)

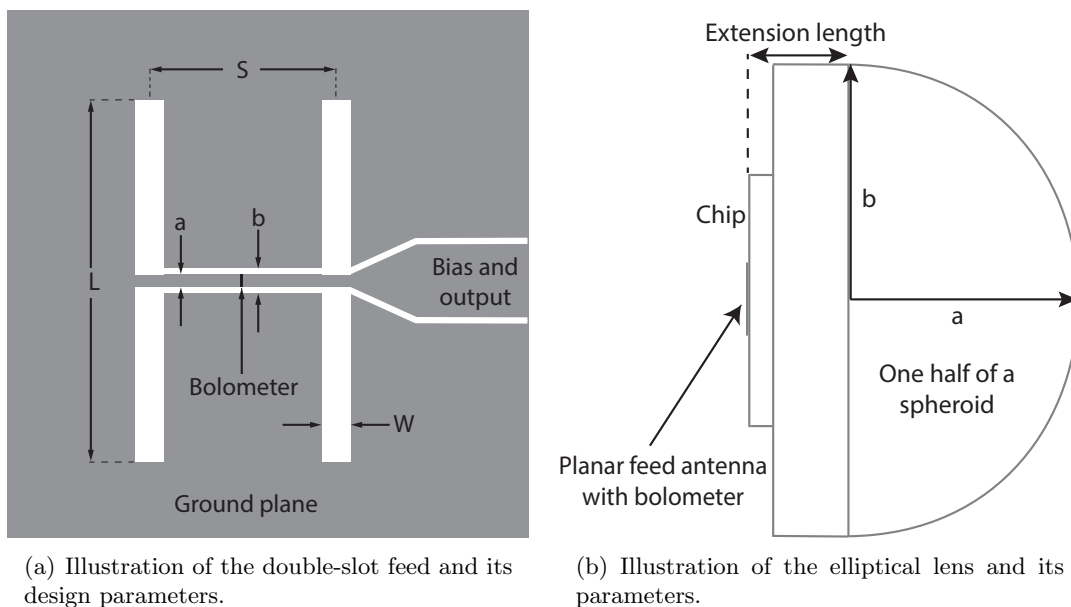


Figure 3.3: Explanation of the dimensions found in table 3.4.

could not be used, instead a curve of the required part of the ellipse was drawn mathematically and then swept in the shape of the lens. The far-field simulations published in the Jellema et al publication [18] were made at 1.1 THz. For good comparison CST MWS was set up for calculations on 1.0 THz – 1.3 THz with the same mesh setting as previous measurements (a mesh density of 12 lines per wavelength and 6 times metal edge mesh refinement). At these high frequencies the $\varnothing = 5$ mm silicon ($\epsilon_r = 11.7$) lens becomes electrically very large. This resulted in totally 126×10^6 mesh cells even when the two planes of symmetry $E_t = 0$ and $H_t = 0$ were used. The simulation took

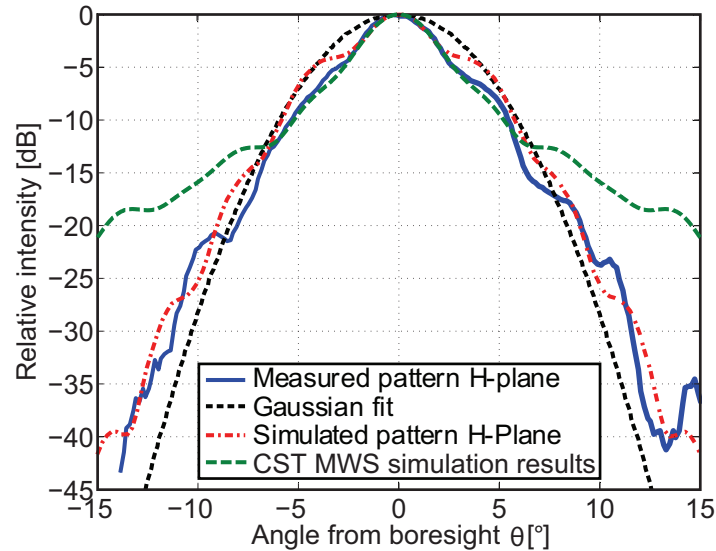


Figure 3.4: Comparison between CST MWS simulation results (green) H-plane and simulated and measured results from publication [18]. All at 1.1 THz.

approximately 60 hours with the accuracy limit set to -30 dB. In figure 3.4 the far-field simulations are plotted together with the measurement and simulation results from the publication. As mentioned in the publication the measurement and simulations done by Jellema et al. agree in the upper 5 dB but the side lobe structure is different below that level. The now performed CST MWS simulation results for the H-plane are in good agreement down to 12 dB which is significantly better but below that level the side-lobe structure looks completely different. The reasons for this were not clearly investigated but one reason can be that most of the lens was surrounded by metal and an absorbing material during the measurements. Also minor differences on the double-slot feed such as bias and signal output structure that are not included in simulations can have an impact on the side-lobes [18].

3.1.3 Elliptical lens and log-spiral feed

For the measurement part, the hybrid antenna consists of an elliptical lens with a log-spiral feed so simulations with these configurations were performed. One of the difficulties with the spiral antenna is that the structure does not have the $E_t = 0$ and $H_t = 0$ symmetry planes which makes the simulations 4 times more demanding than the double-slot antenna simulations. Since the hybrid antennas with diameters of several millimetres become so electrically large, it is not possible to simulate the whole hybrid antenna in CST MWS for the higher frequencies with the available computing power. It was in fact not possible to do a set-up in CST MWS 2012 with 12 lines per wavelength and a $\varnothing = 5$ mm silicon lens above 2 THz in frequency without getting an error message from

CST MWS directly during the set-up. The error message appeared when the number of mesh cells increased to over 2.2 billion. It was later discovered that this limitation had been increased to 100 billion in the later version of CST MWS (2013). But no new simulations were done with this version due to the long simulation time required with the available CPU power. The simulations on the elliptical lens and log-spiral feed were performed at around 500 GHz to avoid the long computing time. The CST MWS set-up of the elliptical lens with a log-spiral feed on the back side can be found in figure 3.5. Simulations were performed with log-spiral feeds of two different dimensions.

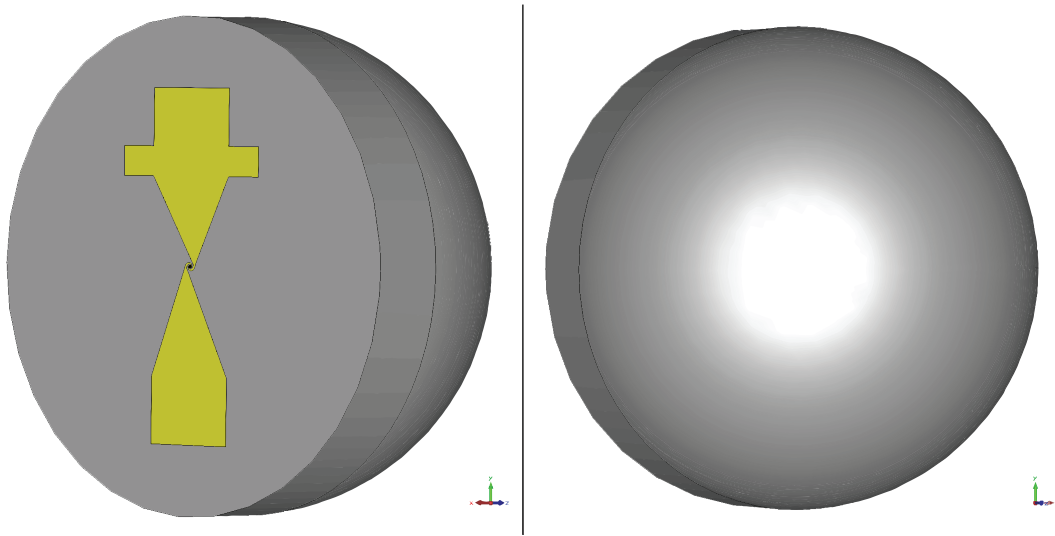
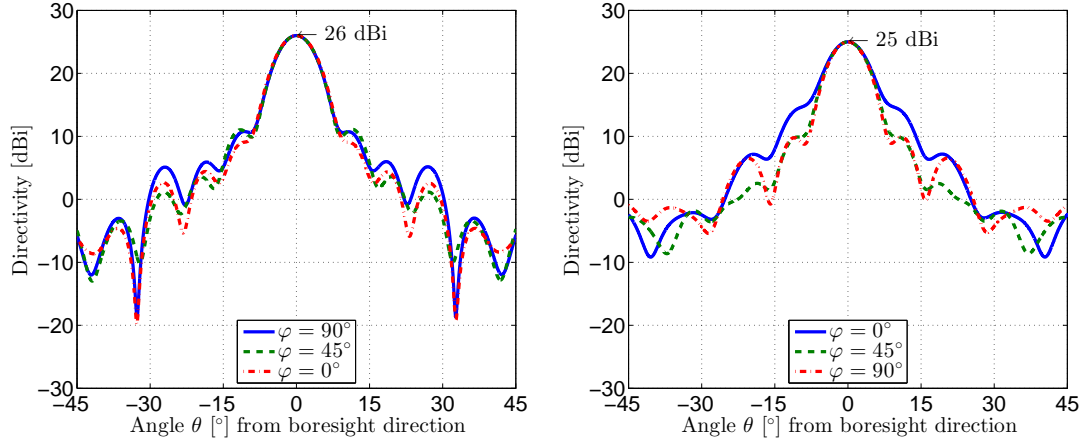


Figure 3.5: The back side (left) and the front side (right) of the hybrid antenna used in the CST MWS simulations. On the back the antenna contacts are visible but the spiral is too small to be distinguished.

First with a spiral with outer diameter $D = 100 \mu\text{m}$ and inner diameter $d = 7 \mu\text{m}$ and then with a spiral with outer diameter $D = 200 \mu\text{m}$ and inner diameter $d = 14 \mu\text{m}$. The designations referring to figure 2.4. The dimensions of the elliptical lens were the same as the dimensions given in table 3.4. The calculated far-field pattern from the simulation can be found in figure 3.6. For the rest of the thesis work the dimensions $D = 100 \mu\text{m}$ and $d = 7 \mu\text{m}$ were used for the log-spiral feed.

3.1.4 The diagonal horn

The WR-2.2 diagonal horn that will be used on the RF source was modelled in CST MWS according to specifications in appendix C and then simulated. The resulting far-field pattern can be found in figure 3.7.



(a) The far-field pattern of the hybrid antenna with a $\varnothing = 5$ mm elliptical lens and a $\varnothing = 100$ μm spiral.

(b) The far-field pattern of the hybrid antenna with a $\varnothing = 5$ mm elliptical lens and a $\varnothing = 200$ μm spiral.

Figure 3.6: The far-field pattern of the hybrid antennas at the 3 φ -planes, $\varphi = 0^\circ$, $\varphi = 45^\circ$ and $\varphi = 90^\circ$ for θ -angles from $\theta = -45^\circ$ to $\theta = 45^\circ$.

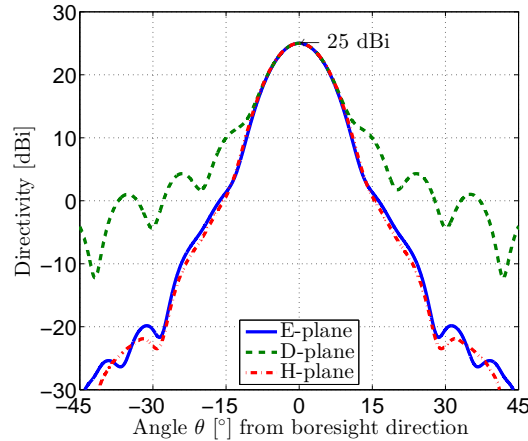


Figure 3.7: The far-field pattern of the VDI's WR-2.2 diagonal horn antenna at the 3 φ -planes, $\varphi = 0^\circ$, $\varphi = 45^\circ$ and $\varphi = 90^\circ$ for θ -angles from $\theta = -45^\circ$ to $\theta = 45^\circ$.

3.2 ADS momentum simulations

Since CST MWS 2012 could not handle the size of the $\varnothing = 5$ mm elliptical lens for frequencies above 2 THz, some simulations were done in Agilent Advanced Design System momentum, ADS MoM [19]. The ADS MoM simulations are done on a computer with a Intel Core2 quad processor working at 2.83 GHz and with 8 GB RAM memory.

In ADS MoM it is possible to simulate the spiral antenna as a sheet at the interface between an infinite silicon substrate and free space. The idea was to compare the beam

pattern from the spiral antenna simulations with the beam pattern from the double slot antenna simulations, since CST MWS simulations at lower frequencies can be done with both the spiral feed or the slot feed on the 5 mm lens. The pattern from the spiral feed and slot feed with no lens can then be compared in ADS MoM simulations at lower and higher frequencies. If the beam pattern of the double-slot feed and the log-spiral feed look similar into silicon in ADS MoM simulations for example at 500 GHz and then also look similar in CST MWS simulations with a lens it can be assumed that this will be valid even with comparison between CST MWS simulations and ADS MoM simulations at higher frequencies. This means that simulations with a double-slot feed can also be valid for a log-spiral feed. Since the log spiral is 4 times heavier to simulate this can be an advantage.

3.2.1 Problem with ADS MoM simulation

The ADS MoM simulations were inconclusive in the beginning. Later some nonphysical results were found. If the silicon air regions were flipped the beam pattern looked totally different and not just flipped as expected. The reason for his behaviour has not been investigated but there must be some limitations or bug in how ADS MoM does the MoM calculations that gives this nonphysical result. The difference in results can be seen if figure 3.8. For easy comparison of simulation results, it would be preferable to have the air and silicon regions as in figure 3.8(a) since this will give the main beam in the positive Z-direction. These simulations were done at 2.5 THz with only the spiral and not the antenna contacts. If the antenna structure including the contacts were used during simulations the used computer ran out of memory resulting in a simulation error for frequencies above 800 GHz with the default mesh density setting of 20 cells per wavelength. In the proceeding ADS MoM simulation the substrate was placed in the negative Z-direction (figure 3.8(c)) and the coordinates were recalculated using Matlab for easier comparison to the CST MWS results.

3.3 CST MWS and ADS MoM simulation comparison

As mentioned earlier the used computer ran out of memory for simulations above 800 GHz in ADS MoM when contact pads of the spiral were included in the simulations. Simulation time for lower frequencies can also be decreased if only the spiral part of the antenna is used instead of the whole antenna structure with the contacts included. The contact pads may have an effect on the beam pattern at the low frequencies that will be used during measurements (below 500 GHz) since the radiating part of the antenna increases. To investigate the effect this will have on the simulation and measurements results simulations are done with both situations for some frequencies and then the results are compared. Figure 3.9(a) illustrates the log-spiral feed structure with contacts (left) and without contacts (right). Some of these simulations were done after the initial measurements. The reason for the odd frequency used in these simulations was that the RF source had a desired peak in output power at (452.5 GHz) so this frequency was used

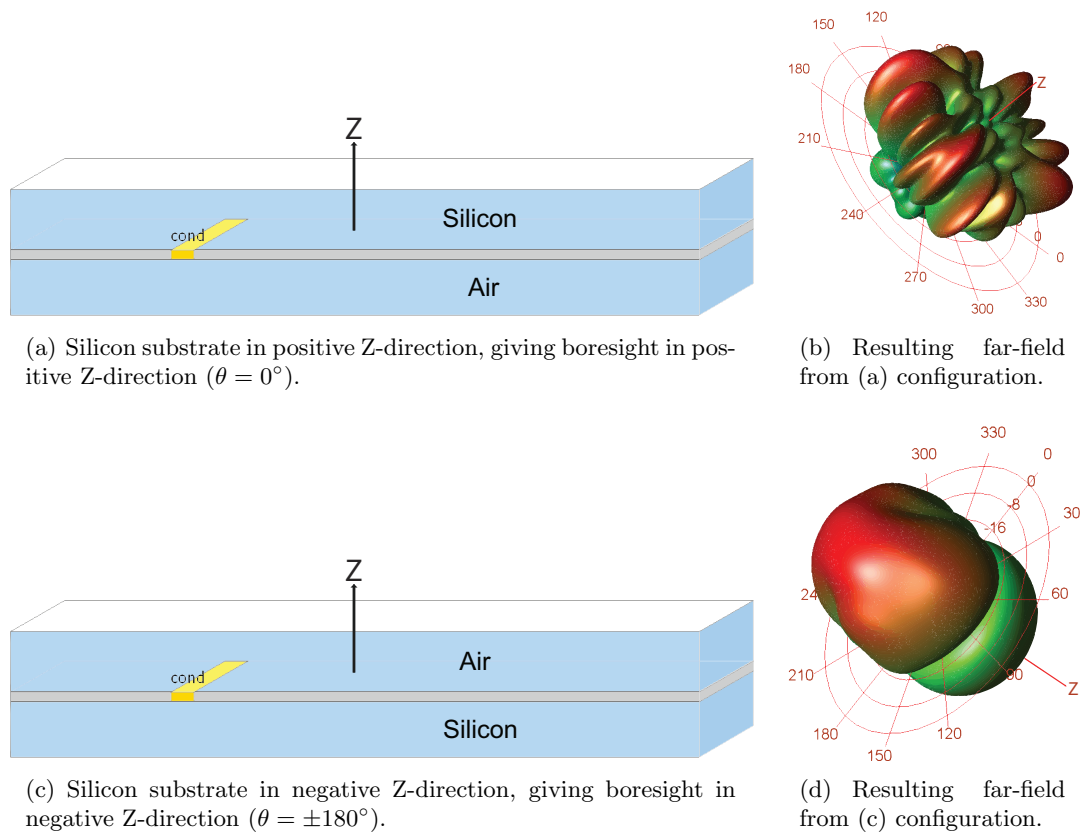


Figure 3.8: The impact in ADS MoM result at 2.5 THz when just flipping the configuration in the coordinate system. (a) is the decried configuration since boresight in positive Z-direction ($\theta = 0^\circ$) which is standard convention and is desired for comparison with other simulations and publications.

during the later measurements (chapter 6).

3.3.1 Directivity comparison

The lens with the log-spiral feed was simulated in CST MWS both with the antenna contact pads included and without the contact pads. The patterns were in good agreement with each other at smaller θ angles despite the absence of the outer parts (contact pads) of the antenna during simulation with the lens included. The first side-lobes at about 15 dB below max were more distinct in the simulations with the contact pads included. A comparison in directivity for 3 different φ -planes for the different situations can be seen in figure 3.9.

Simulations with and without contact pads were also done with Agilent ADS MoM. The differences were more significant in these simulations. The beam pattern in to the silicon were calculated for 3 different planes and can be seen in figure 3.10. No lens

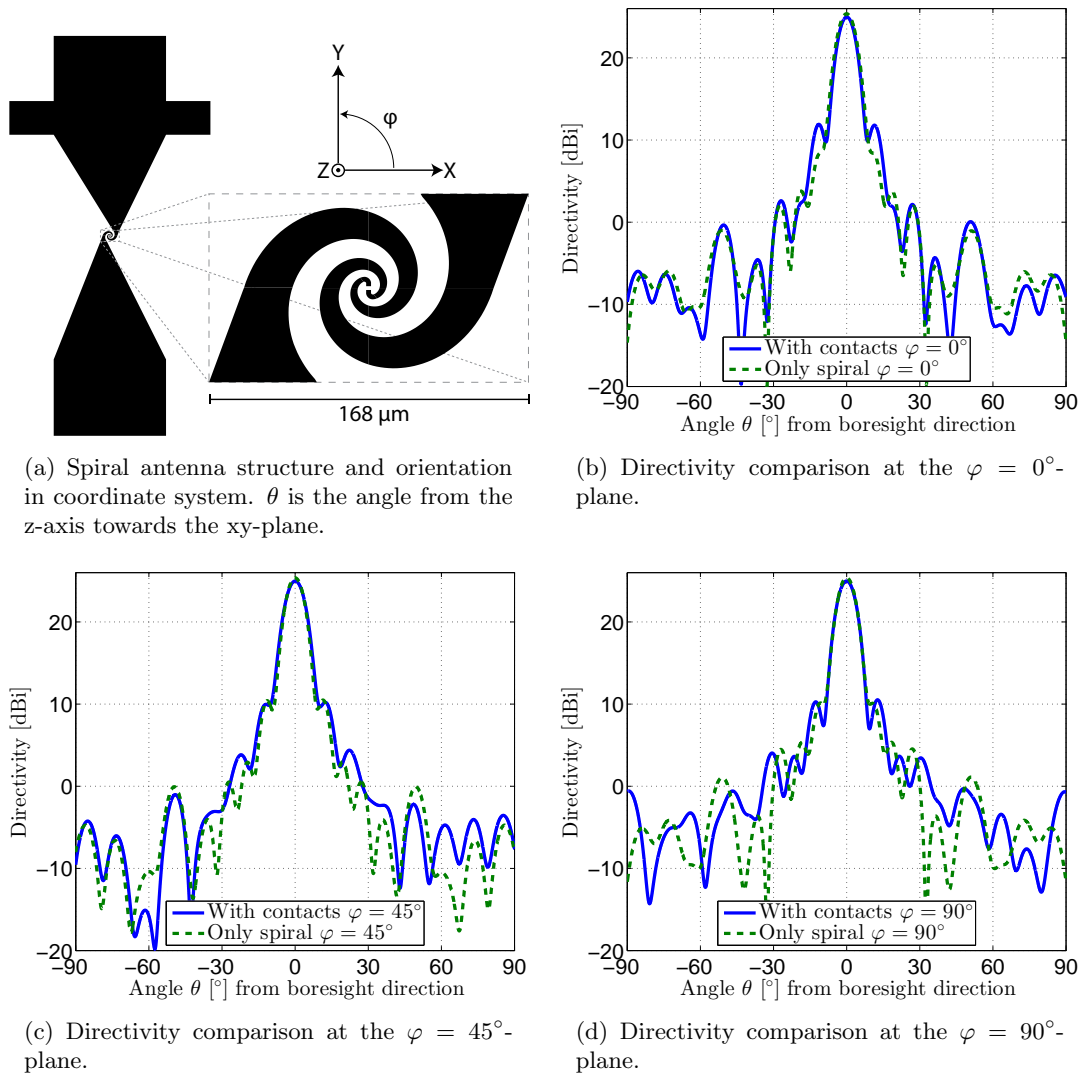


Figure 3.9: CST MWS simulations done with lens and at 452.5 GHz, boresight directivity 26 dB. Comparison between cases when the antenna contacts are included and not included in the simulations.

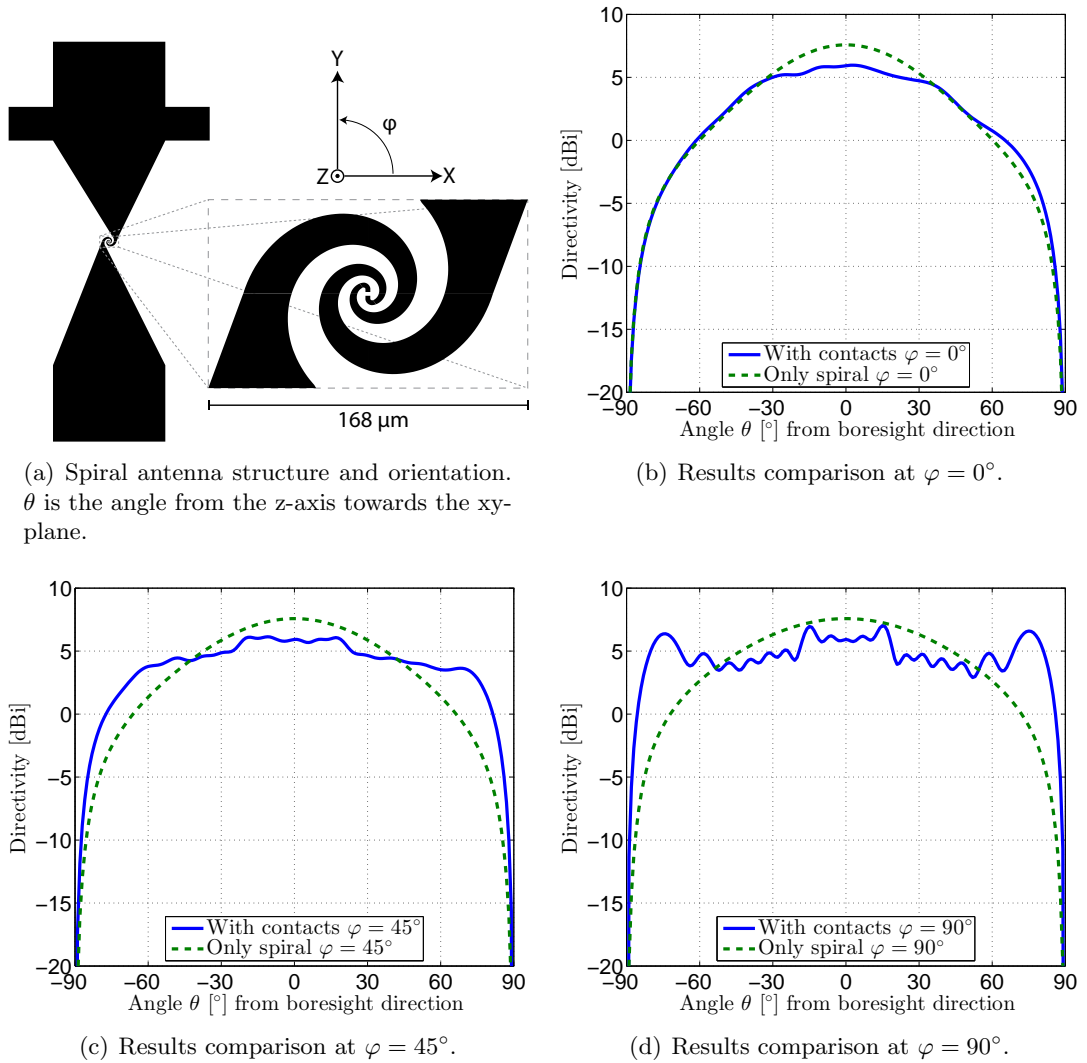


Figure 3.10: The beam pattern in to the silicon from ADS MoM simulations done at 452.5 GHz. Comparison between cases when the antenna contacts are included and not included in the simulations. No lens can be included in the ADS MoM simulations.

was included in the simulation. It was clear that when φ approaches 90° (the plane along the antenna contacts) the beam becomes wider and more uneven. This could be related to the aforementioned mentioned problems with ADS MoM simulations and uneven patterns since the differences were not that large in the CST MWS simulations. The contact pads seems to have an effect on how the beam pattern looks in to the silicon. The lens compensate for the differences in the main lobe but the side lobe patterns looks different. This means that the contact pads does not have to be included for simulations intended to be used for Gaussian fit with only the fundamental mode.

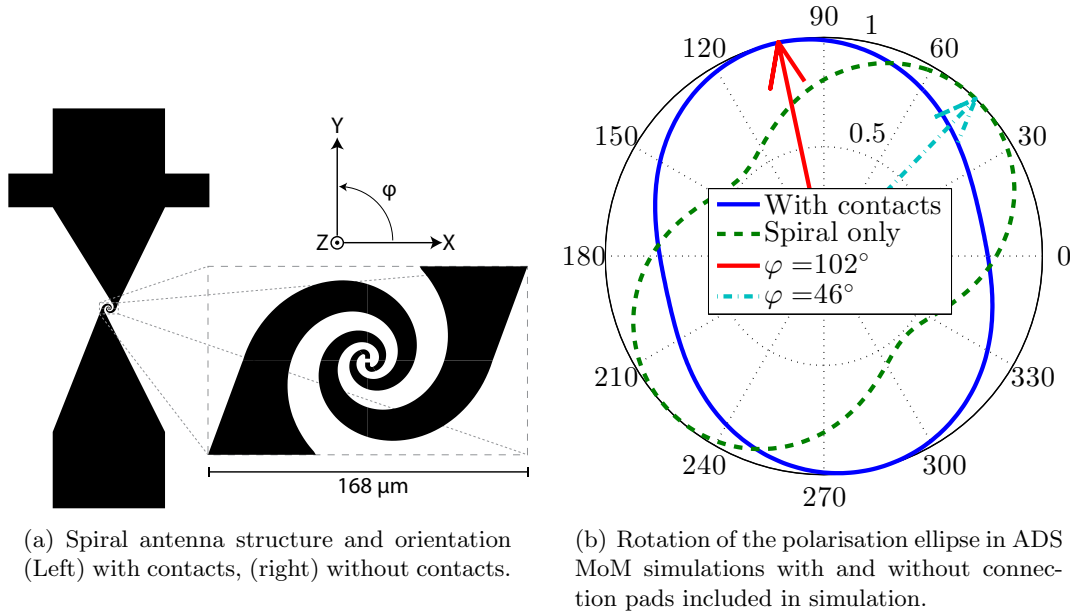


Figure 3.11: Figure (b) shows the polarisation ellipse in relation to the structure (a) when ADS MoM simulations at 452.5 GHz are done with $AR = 2.7$ dB and then without $AR = 5.6$ dB the contacts. No lens was included in these simulations.

3.3.2 The contact pads' impact on the polarisation

Since the log-spiral feed was used for the rest of the simulations and the measurements it had to be considered that the radiation from the log-spiral antenna is elliptically polarised. To get the best coupling between the elliptical polarisation of spiral antenna and the linear polarisation of the horn antenna, both the direction of the polarisation ellipse and the Axial Ratios AR are of interest. The Axial Ratio is the ratio between the orthogonal E-fields components. For circular polarisation the Axial Ratio is 1 or 0 dB. A linear polarised field has infinite Axial Ratio since it does not have an orthogonal component. To find the polarisation ellipse orientation of the beam, the θ angle is fixed in the boresight direction of the simulated pattern. This means $\theta = 0^\circ$ for the CST MWS simulations and $\theta = \pm 180^\circ$ for the ADS MoM simulations. Then φ is swept from 0 to 360° . If we look at E_φ -field component or E_θ -field component they will have their maximum values when the electrical field is tangential with their coordinate axis. This relation gives that the angle φ that corresponds to the maximum E_θ value is also the angle from the X-axis of the coordinate system to the major axis of the polarisation ellipse. See figure 3.11.

Figure 3.11(b) shows the polarisation simulation result from the ADS MoM. To be able to simulate without a lens in CST MWS the background material was set to silicon and an air box with open boundary conditions was placed behind the antenna to represent the air. The result for CST MWS simulations can be found in figure 3.12(b).

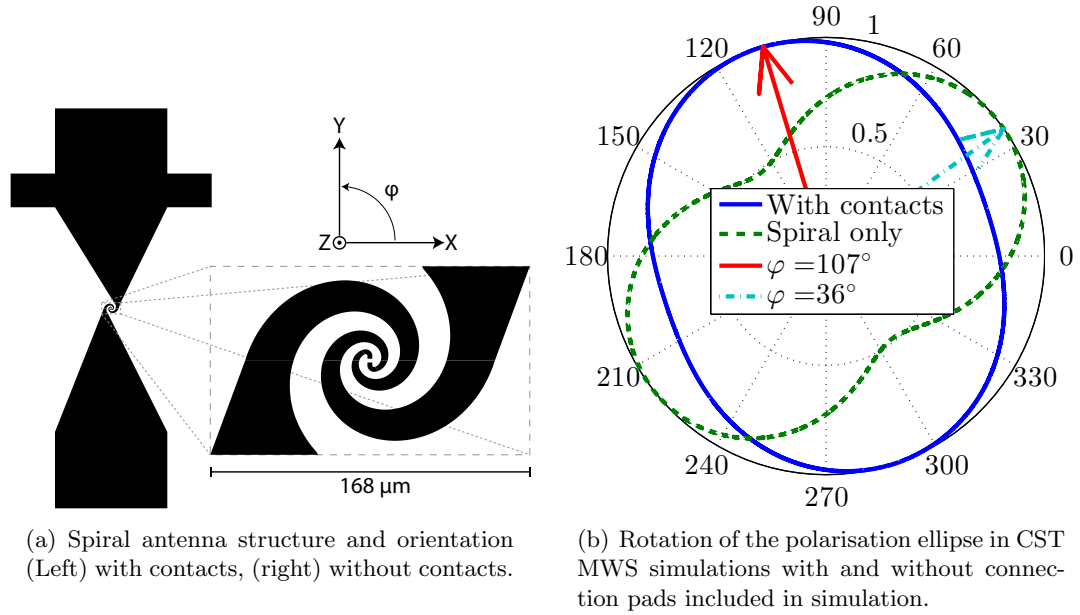


Figure 3.12: Figure (b) shows the polarisation ellipse in relation to the structure (a) when CST MWS simulations at 452.5 GHz are done with $AR = 2.3$ dB and then without $AR = 6.3$ dB the contacts. No lens was included in these simulations.

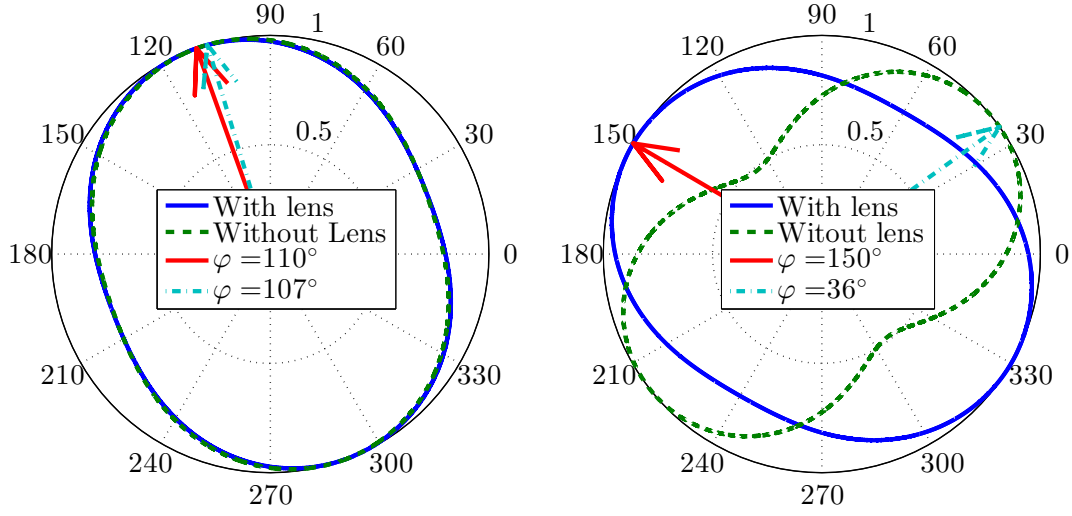
Table 3.5: Summation of the contact pads' impact on the polarisation ellipse for the simulations done without a lens included.

Formation	Parameter	Simulation program used	
		ADS MoM	CST MWS
With contact pads	E-field axial ratio	2.7 dB	2.3 dB
	Polarisation ellipse orientation	$\varphi = 102^\circ$	$\varphi = 107^\circ$
Without contact pads	E-field axial ratio	5.6 dB	6.3 dB
	Polarisation ellipse orientation	$\varphi = 46^\circ$	$\varphi = 36^\circ$

The simulations indicated that the polarisation ellipse rotates when the contact pads are removed in the simulation set-up. The results from the ADS MoM and CST MWS simulations without lens are summarised table 3.5. The AR indicates that the polarisation becomes more circular when the contact pads are included in the simulations. The reason for this is rather unclear.

3.3.3 The lens impact on the polarisation

The lens effect of the polarisation was also investigated. Simulations with the lens was done with contact pads (figure 3.13(a)) and without contact pads (figure 3.13(b)). The



(a) The polarisation ellipse with contact pads included. The removal of the lens introduced a 3° ellipse shift and no significant change in AR 2.3 dB.

(b) The polarisation ellipse with contact pads not included. The removal of the lens introduced a 96° or 114° ellipse shift and change in AR from 2.5 dB to 6.3 dB.

Figure 3.13: The lens impact on the polarisation when antenna contacts are included (a) or not (b) in the simulations at 452.5 GHz.

Table 3.6: Summation of the contact pads' impact on the polarisation ellipse for the simulations done with the lens included.

Formation	Parameter	With Lens	Without Lens
With contact pads	E-field axial ratio	2.3 dB	2.3 dB
	Polarisation ellipse orientation	$\varphi = 110^\circ$	$\varphi = 107^\circ$
Without contact pads	E-field axial ratio	2.5 dB	6.3 dB
	Polarisation ellipse orientation	$\varphi = 150^\circ$	$\varphi = 36^\circ$

addition of the lens to the simulations had a minor effect on the polarisation ellipse when the contacts was included in the simulations. The simulation comparison gave a shift of 3° in orientation and no significant change in AR between simulations with and without the lens (figure 3.13(a)). The lens influence on the polarisation was larger when the contact pads were removed in the simulations 3.13(b). In this case the lens makes the radiation more circular, from 6.3 dB to 2.5 dB in axial ratio and rotates the polarisation ellipse 114° or 96° . The results are summarised in table 3.6.

4

Parameter extraction

The first part of this chapter describes the method used to extract the Gaussian beam parameters from the simulation data. Then a short discussion of the phase centre extraction.

4.1 Gaussian fit of far-field patterns

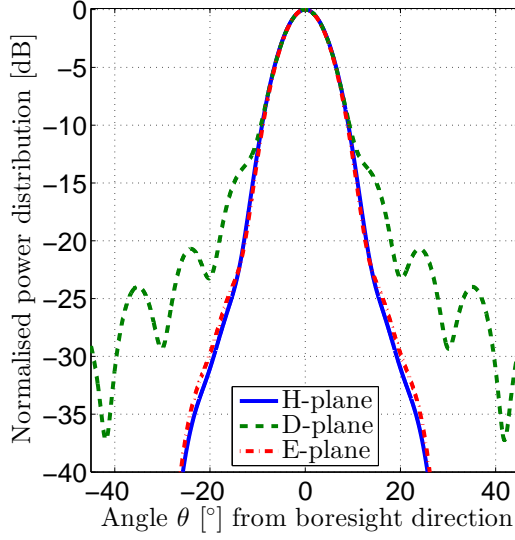
From the far-field patterns obtained with CST MWS (figure 4.1), the Gaussian beam parameters were extracted using Matlab and equations from section 2.4. The beam waists were estimated with two different methods. This gave the possibility to compare the results and see if method 1 is sufficient to use in these cases.

4.1.1 Method 1: From the 3 dB beam width

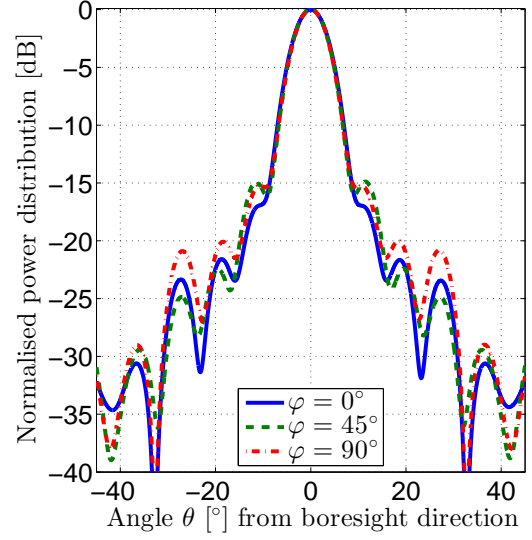
The 3 dB angular beam width or Full Width at Half Maximum (FWHM) angle of a far-field pattern describes the angular width θ_{fwhm} between the points where the power has dropped to half the value of boresight (figure 4.2). For a Gaussian beam the angle can be expressed as $\theta_{3\text{dB}} = \theta_{fwhm} = 1.18 \theta_0$ in which θ_0 is the far-field divergence angle [13]. Using the small angle approximation the far-field divergence angle from equation (2.11) can be simplified to (4.1) if the angle is expressed in radians.

$$\theta_0 \cong \frac{\lambda}{\pi w_0} \quad (4.1)$$

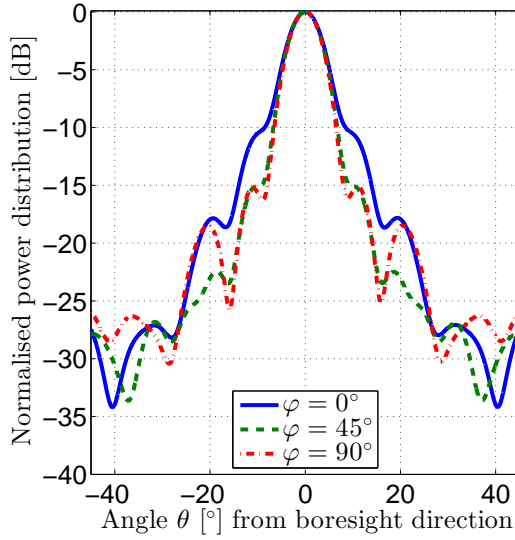
This gives an expression of the beam waist radius w_0 from the 3 dB beam-width angle $\theta_{3\text{dB}}$ with equation (4.2). The quotient $\frac{180}{\pi}$ is used since CST MWS gives the 3 dB beam-width in degrees. Using these equations the beam waists were calculated at the 3 different planes from the far-field pattern plotted in figure 4.1(a) for the diagonal horn and from the far-field pattern plotted in figure 4.1(b) for the hybrid antenna with the $\varnothing = 100 \mu\text{m}$ spiral. The results can be found in table 4.1.



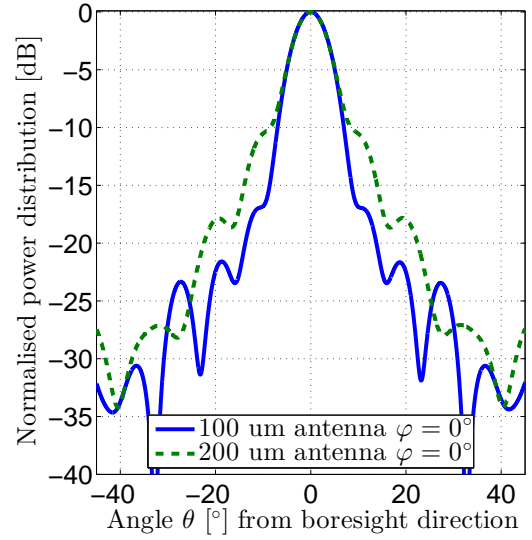
(a) Normalised far-field pattern for the WR-2.2 diagonal horn antenna. Directivity 25 dBi.



(b) Normalised far-field pattern for hybrid antenna with $\varnothing = 5$ mm lens and $\varnothing = 100$ μ m spiral with contacts. Directivity 26 dBi.



(c) Normalised far-field pattern for hybrid antenna with $\varnothing = 5$ mm lens and $\varnothing = 200$ μ m spiral with contacts. Directivity 25 dBi.



(d) Comparison at $\varphi = 0^\circ$ with a $\varnothing = 5$ mm lens between a $\varnothing = 100$ μ m and $\varnothing = 200$ μ m log-spiral feed.

Figure 4.1: The normalised far-field patterns for the WR-2.2 diagonal horn and the $\varnothing = 5$ mm hybrid antenna calculated with CST MWS simulations at 500 GHz.

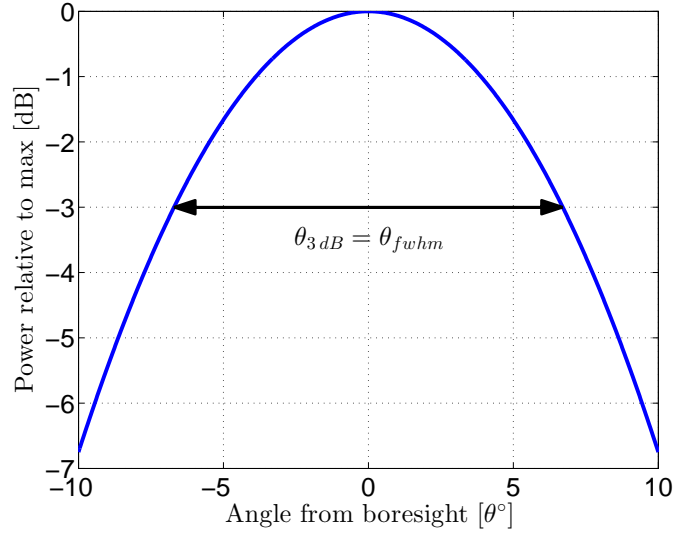


Figure 4.2: The 3 dB beam width or FWHM width is the angular width of the main beam in between where the power are above half the power (3 dB) at max (boresight).

$$w_0 = \frac{1.18 \lambda 180}{\pi \theta_{3 \text{ dB}} \pi} \quad (4.2)$$

Table 4.1: Beam waist radius for the diagonal horn and the hybrid antenna with the $\varnothing = 100 \mu\text{m}$ spiral calculated from the 3 dB beam-width (FWHM) at 500 GHz, $\lambda = 0.6 \text{ mm}$.

Plane angle	3 dB beam-width		Beam waist radius w_0	
	Horn	Hybrid	Horn	Hybrid
$\varphi = 0^\circ$	10.1°	7.3°	1.28 mm	1.77 mm
$\varphi = 45^\circ$	10.1°	7.5°	1.28 mm	1.72 mm
$\varphi = 90^\circ$	10°	7.4°	1.29 mm	1.74 mm

4.1.2 Method 2: Using Gaussian fit with Matlab

The relative power distribution of the fundamental Gaussian beam transverse to the axis of propagation can be expressed as equation (4.3),[13].

$$\frac{P(r)}{P(0)} = \exp \left[-2 \left(\frac{r}{w(z)} \right)^2 \right] \quad (4.3)$$

MathWorks Matlab [20] has a fit function "Gauss1" that fits data points to equation (4.4).

$$f(x) = \exp \left[- \left(\frac{x - b1}{c1} \right)^2 \right] \quad (4.4)$$

If $b1 = 0$, $f(x) = \frac{P(r)}{P(0)}$ and $x = r$ a relation between the parameter $c1$ and the beam width $w(z)$ can be found. This relation was found to be $w = \sqrt{2}(c1)$. Since a fit to the fundamental mode of a Gaussian beam was of interest, only the main beam was used for fitting. In figure 4.1(b) the side lobe level is around -15 dB so only the parts above -15 dB were used for the fit. The relative power distributions down to -15 dB for the 3 different planes from the far-field pattern in figure 4.1(a) for the diagonal horn and from the far-field pattern in figure 4.1(b) for the hybrid antenna were used. The far-field data points for each plane were fitted to equation (4.4). The $c1$ parameter was extracted for each case and multiplied by $\sqrt{2}$, giving the beam radius for each plane cut at the selected far-field distance $z = 1$ m. For simplicity the far-field distance 1 m was used, giving $r = \tan \theta$. $z = 1$ m was in the far-field since $z \gg z_c$ was fulfilled since the confocal distance was the $z_c \approx 9$ mm for the horn antenna and $z_c \approx 16$ mm for the hybrid antenna according to equation (2.10). Then the beam waist radius w_0 for each case was calculated with equation (4.5). Equation (4.5) was derived from equation (2.7) together with equation (2.10) and then the beam waist w_0 was extracted.

$$w_0^2 = \frac{w^2}{2} \left[1 \pm \sqrt{1 - \left(\frac{2\lambda z}{\pi w^2} \right)^2} \right] \quad (4.5)$$

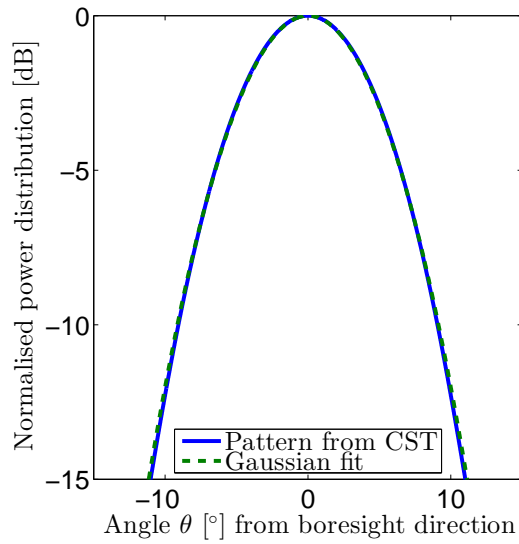
The calculated beam waist radius for the horn and hybrid antennas can be found in table 4.2. A comparison between the far-field pattern and the estimated Gaussian distribution for the horn and hybrid antennas is plotted in figure 4.3 and 4.4 respectively.

Table 4.2: Beam waist radius for the diagonal horn and the hybrid antenna with the $\varnothing = 100 \mu\text{m}$ spiral from the Gaussian fit of far-field with Matlab.

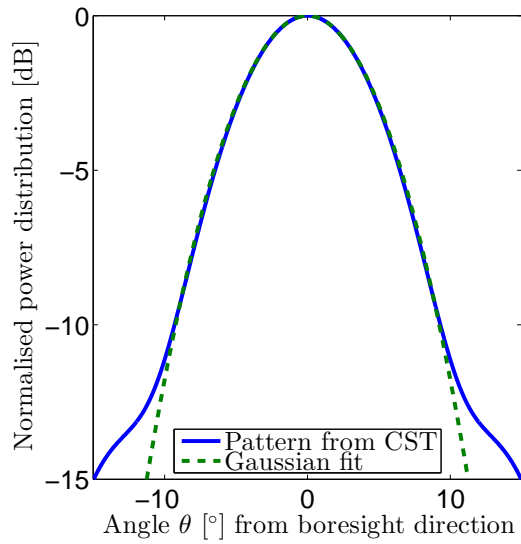
Plane angle	Beam waist radius w_0	
	Horn	Hybrid
$\varphi = 0^\circ$	1.27 mm	1.74 mm
$\varphi = 45^\circ$	1.26 mm	1.73 mm
$\varphi = 90^\circ$	1.30 mm	1.77 mm

4.1.3 Comparison results from different methods

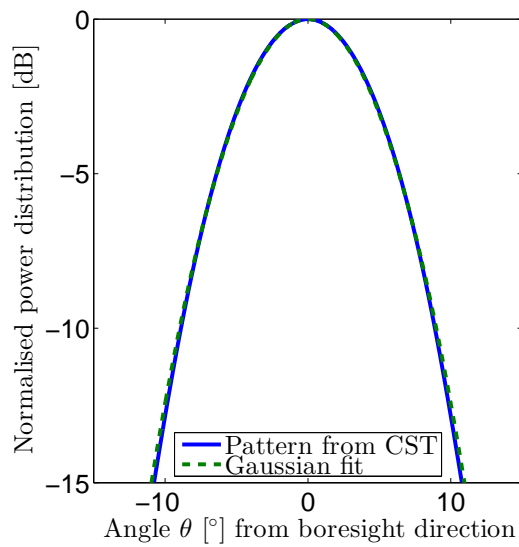
The extraction of the beam waist with two different methods gave consistent results. This gives that the Gaussicity is high in the region used for the extraction $\theta \approx \pm 10^\circ$.



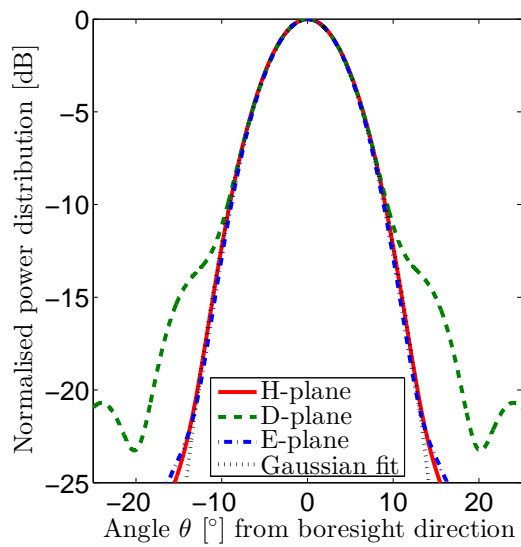
(a) Comparison at $\varphi = 0^\circ$ (H-plane), $w_0 = 1.27$ mm, $\theta_0 = 8.6^\circ$.



(b) Comparison at $\varphi = 45^\circ$, $w_0 = 1.26$ mm, $\theta_0 = 8.7^\circ$.



(c) Comparison at $\varphi = 90^\circ$ (E-plane), $w_0 = 1.29$ mm, $\theta_0 = 8.4^\circ$.



(d) Comparison at all 3 planes with $w_0 = 1.28$ mm.

Figure 4.3: Gaussian fit down to a power level of -15 dB below max and simulated far-field power pattern for the horn antenna.

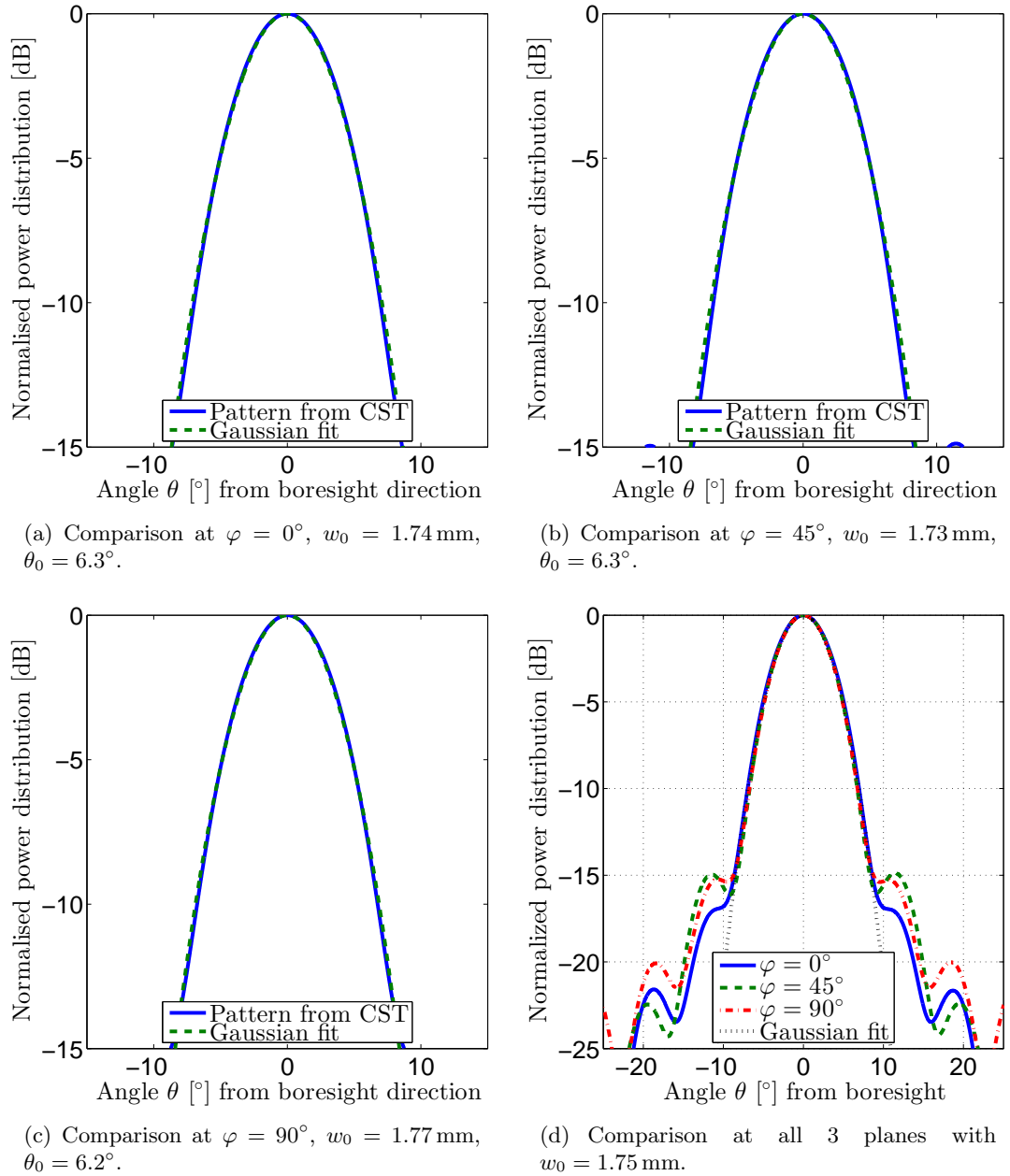


Figure 4.4: Gaussian fit down to a power level of -15 dB below max and simulated far-field power pattern for the hybrid antenna.

Table 4.3: Comparison between extracted beam waist sizes w with the two different methods for the horn antenna.

Extraction method	Calculated beam waist size w_0		Difference Δ [mm]
	FWHM	Gaussian fit	
Plane angle			
$\varphi = 0^\circ$	1.28 mm	1.27 mm	0.01
$\varphi = 45^\circ$	1.28 mm	1.26 mm	0.02
$\varphi = 90^\circ$	1.29 mm	1.30 mm	0.01

The extracted beam waist $w_0 \approx 1.3$ mm for the diagonal horn is also what the manufacture [11] specified. The manufacture specification for the WR-2.2 diagonal horn can be found in appendix C.

Table 4.4: Comparison between extracted beam waist sizes w with the two different methods for the hybrid antenna.

Extraction method	Calculated beam waist size w_0		Difference Δ [mm]
	FWHM	Gaussian fit	
Plane angle			
$\varphi = 0^\circ$	1.77 mm	1.74 mm	0.03
$\varphi = 45^\circ$	1.72 mm	1.73 mm	0.01
$\varphi = 90^\circ$	1.74 mm	1.77 mm	0.03

4.2 The phase centre position

The position of the phase centre is a parameter that is needed to determine where the focal point on the mirror should be relative to the horn or hybrid antenna. The phase centres can be extracted from CST MWS directly. The phase centre is statistically estimated from calculations out to an angle θ away from boresight direction. The phase centre position is given in Cartesian coordinates in the global coordinate system of CST MWS. Since there is an uncertainty in the calculations of the phase centre a standard deviation σ is also given. For the horn antenna the phase centre was given to be at 3 mm behind the edge of the horn aperture with a standard deviation $\sigma = 0.5$ mm when the calculations are done out to $\theta = 10^\circ$. For the hybrid antenna the phase centre was given to be around 14 mm behind the tip of the lens. The standard deviation σ was 10 mm so the position is very uncertain.

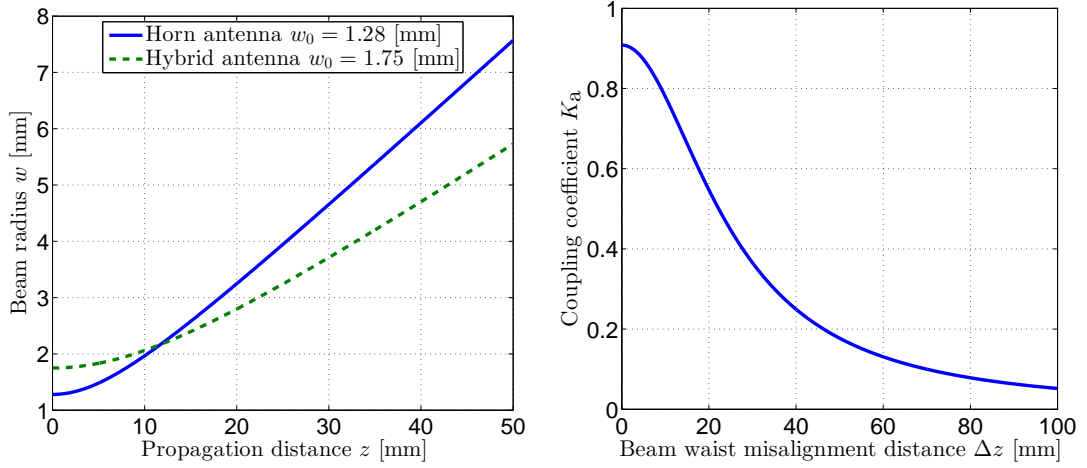
5

Measurement system implementation

The chapter starts with comparison of Gaussian beam parameters from the horn and hybrid antenna and how they will couple the RF radiation without a quasi-optical waveguide. The chapter ends with a description of the quasi-optical waveguide design.

5.1 Coupling between the antennas

As seen in the previous section the beam waist was not the same for both antennas. The average value for the beam waists that were extracted from the 3 planes were $w_{0,\text{horn}} \approx 1.28$ mm for the horn antenna and $w_{0,\text{hybrid}} \approx 1.75$ mm for the hybrid antenna. The beam waist of the horn was smaller than the beam waist of the hybrid antenna. This made the beam from the horn antenna more divergent than the beam from the hybrid antenna. This can be seen in figure 5.1(a) in which the beam widths (equation 2.7) are plotted as a function of propagation distance z . The confocal distances for the corresponding beams are given by equation 2.10 to be $z_{c,\text{horn}} \approx 9$ mm and $z_{c,\text{hybrid}} \approx 16.0$ mm. The far-field divergence angles were calculated with equation (4.1) to be $\theta_{0,\text{horn}} \approx 8.5^\circ$ and $\theta_{0,\text{hybrid}} \approx 6.3^\circ$. It is clear from the figure that the beam from the horn antenna cannot be effectively coupled to the hybrid antenna without any refocusing element. One possibility would be to put the diagonal horn and the hybrid antenna directly against each other. According to the simulations with CST MWS the phase centre of the hybrid antenna is about 14 mm behind the lens surface and the phase centre of the diagonal horn is about 3 mm behind the aperture. This fact makes it impossible to put the beam waists at the same position. In figure 5.1(b) the coupling coefficient K_a from equation (2.17) is plotted against the misalignment distance Δz when $w_{0a} = w_{0,\text{horn}} = 1.28$ mm and $w_{0b} = w_{0,\text{hybrid}} = 1.75$ mm. If the positions of the beam waists could be aligned at a common position the coupling would still be about 90%. If the beam waists were assumed



(a) The Gaussian beam radius when propagating away from the horn and hybrid antennas respectively.

(b) Coupling coefficient for the diagonal horn antenna and hybrid antenna versus the Δz misalignment distance.

Figure 5.1: Effect on the coupling coefficient K_a when mismatched in waist size or waist position along axis of propagation.

to be at the phase centre locations the distance between them would be $\Delta z \approx 17$ mm giving a coupling around 60% if the antennas would be placed as close as physically possible.

5.2 Quasi-optical waveguide design

To get a better coupling between the antennas lenses or mirrors can be used. Since the beam waist for the horn antenna was $w_{0,\text{horn}} \approx 1.28$ mm and the beam waist for the hybrid antenna was $w_{0,\text{hybrid}} \approx 1.75$ mm a lens or mirror system with a magnification of $\mathfrak{M} \approx 1.37$ given by equation (2.13) was desired.

5.2.1 With two parabolic mirrors

To couple the radiation from the horn antenna to the hybrid antenna, two parabolic mirrors can be used in a configuration as in figure 5.2. When this U-configuration is used the off-axis aberrations described earlier will be minimized [21]. With this configuration, the distortions introduced given by equation (2.14) and (2.15) produced by the first mirror will be cancelled out by the second mirror if the mirrors are identical. The phase slippage between the mirrors will still be present and is given by equation (5.1) so the distance between the mirrors matters.

$$\Delta\phi_{1,2} = \arctan\left(\frac{\lambda(d_2 + d'_1)}{\pi w_{02}^2}\right) - \arctan\left(\frac{\lambda d_2}{\pi w_{02}^2}\right) \quad (5.1)$$

What the different parameters used in equation (5.1) represent can be found in figure 5.2. If the focal length of the parabolic mirror is the same as the radius of curvature of the incident beam, the output waist will occur at the mirror plane. However if the source beam waist w_0 is placed at the focal point, the second waist will occur beyond the mirror [22]. So if the second waist $w_{02} = \mathbf{W}_{02}$ occurs at the second mirror \mathbf{M}_2 giving $d'_1 = 0$ in equation (5.1) the phase slippage will be $\Delta\phi_{1,2} \approx 0$ [14]. The magnification is a relation between the input and output beam waists according to equation (2.13). Longer focal length hence longer distance from antenna gives broader beam waist at the mirror. If the beam waist at the mirrors is large in relation to the wavelength, the Far-field divergence angle θ_0 will be small according to equation (4.1). This means that the beam divergence can be neglected for shorter distances between the mirrors. If a magnification for each mirror is chosen so the beam waist at each mirror surface becomes the same there should be a good coupling between the antennas. If the relation $\mathfrak{M} \approx 1.37$ given by equation (2.13) is used for the focal lengths of the mirrors and hence also the distance to the antennas beam waists, the new beam waists sizes at the mirrors will be the same for both mirrors. This will also make the system more wavelength independent [13]. One proposed configuration can be found in table 5.1.

Table 5.1: Design parameters for system with 2 parabolic mirrors 25 cm apart.

Parameter name	Parameter	Parameter values
Total magnification	$\mathfrak{M}_{\text{sys}}$	1.37
Focal length mirror \mathbf{M}_1	$f_{\mathbf{M}_1}$	110 mm
Focal length mirror \mathbf{M}_2	$f_{\mathbf{M}_2}$	150 mm
Magnification mirror \mathbf{M}_1	$\mathfrak{M}_{\mathbf{M}_1}$	12.82
Magnification mirror \mathbf{M}_2	$\mathfrak{M}_{\mathbf{M}_2}$	9.35
Beam waist at mirror \mathbf{M}_1	$w_{0\mathbf{M}_1} \approx \mathbf{W}_{02}$	16.45 mm
Beam waist at mirror \mathbf{M}_2	$w_{0\mathbf{M}_2} \approx \mathbf{W}_{02}$	16.46 mm
Beam divergence angle mirror $\mathbf{M}_1 \rightarrow \mathbf{M}_2$	θ_0	0.67°
Coupling coefficient	K_a	$0.9995 \approx 1$

We see in table 5.1 that the beams are not perfectly matched but the mismatch is so low that the effect on the coupling efficiency can be neglected in this context. With this configuration, the mismatch introduced by the off-axis configuration will cancel out [14]. There can still be coupling losses if the new beam waist after the second mirror does not match the hybrid antennas beam waist in size and position. This loss is given by a coupling coefficient calculated with equation (2.17). As an example if $w_{0,b} = \mathbf{W}_{01}$ is chosen to be the beam waist of the horn antenna, $w_{0,a} = \mathbf{W}_{03}$ is the beam waist produced by mirror \mathbf{M}_2 and Δz the misalignment in propagation direction \mathbf{d}'_2 of the beam waists in figure 5.2. There will also be coupling losses if the beams not are aligned

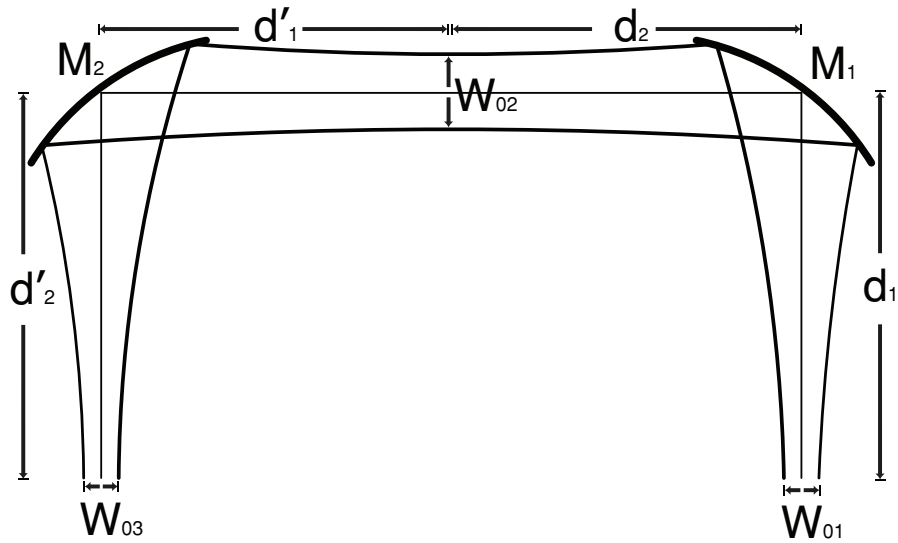


Figure 5.2: A possible set-up with two parabolic mirrors.

or tilted in other directions but we assume that these errors can be adjusted during measurements. A shift of beam waist size and position can also occur with a change in frequency depending on the antennas. The complex beam parameters and the ABCD law from [13] can be used to calculate the beam widths at any point in the quasi-optical system. Figure 5.3 illustrates how the beam width between the horn and hybrid antenna changes when the beam propagates through a quasi-optical waveguide designed with the parameters from table 5.1.

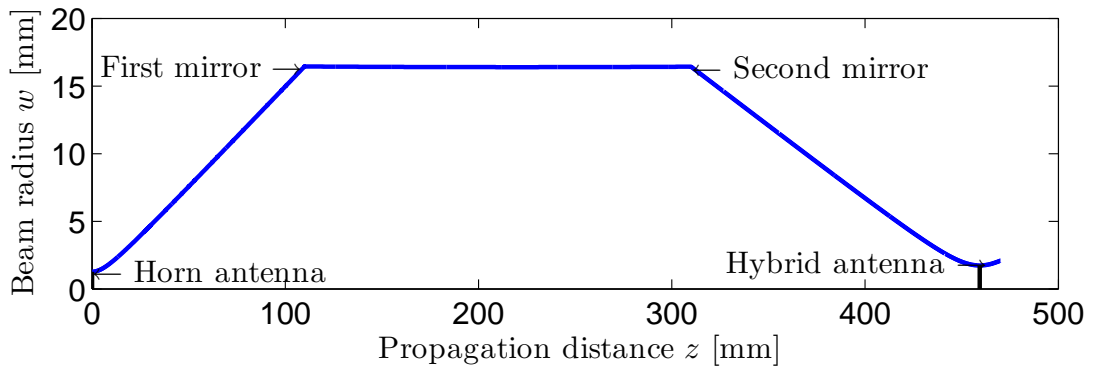


Figure 5.3: The Gaussian beam radius variation when propagating from the horn antenna to the hybrid antenna through Quasi-optical system with two parabolic mirrors.

5.2.2 Using one elliptical mirror

The design procedure for the elliptical mirror is taken from [13]. Since the desired input and output waist sizes are known, the magnification \mathfrak{M} is given by equation (2.13). With the magnification a focal length f_e can be calculated for a chosen input distance d_{in} with equation (5.2) in which $\mathfrak{N} = 1 - \mathfrak{M}^{-2}$.

$$f_e = z_c \left(\frac{d_{\text{in}}}{\mathfrak{N}z_c} \right) \left[1 - \sqrt{\left(1 - \mathfrak{N} \left[1 + \left(\frac{d_{\text{in}}}{z_c} \right)^{-2} \right] \right)} \right] \quad (5.2)$$

To achieve minimum distortion, the distances from each focal point R_1 and R_2 to the centre point P of the used portion of the ellipse (see figure 5.4) should be selected to be the radius of curvature of the each beams respectively. The chosen input distance d_{in} gives R_1 with equation (2.8) which then together with f_e can be used in equation (5.3) to calculate R_2

$$R_2 = \frac{f_e R_1}{R_1 - f_e} \quad (5.3)$$

R_1 and R_2 give the length of the major axis $R_1 + R_2 = 2a$. For a desired reflection angle $2\theta_i$, the eccentricity of the ellipse can be calculated with equation (5.4). When the eccentricity is known the minor axis length is given by $2b = 2a\sqrt{1 - e^2}$ and the focal points separation by $A_0 = 2ea$

$$e = \frac{\sqrt{R_1^2 + R_2^2 - 2R_1R_2 \cos 2\theta_i}}{R_1 - R_2} \quad (5.4)$$

Two proposed set-ups with one elliptical mirror and the calculated parameters for the diagonal horn and the hybrid antenna can be found in table 5.2.

5.2.3 Edge taper of proposed systems

A mirror diameter of $4w$ gives an edge taper of 34.7 dB and corresponds to a mirror diameter of $4 \cdot 16.46 \approx 66$ mm for the system example with two parabolic mirrors in table 5.1. For the configurations with the elliptical mirrors (table 5.2) the given mirror diameters are 60 mm and 90 mm respectively.

5.2.4 Choice of mirrors and configuration

For the real physical system mirrors needed to be available from stock. Elliptical curved mirrors with the required dimension and cut cannot be purposed from stock and need to be customary fabricated. For the two off-axis mirror set-up, mirrors with the proposed focal lengths are not available but mirrors with dimensions near the desired values can be chosen and then the mismatch can be calculated. As discussed above for the parabolic mirror set-up, a relation between the focal length of the mirrors equal to the magnification $\mathfrak{M}_{\text{horn} \rightarrow \text{hybrid}} = 1.37 = \frac{f_{\text{hybrid}}}{f_{\text{horn}}}$ is desired. At Edmund Optics two pairs of

Table 5.2: Design parameters for elliptical mirror relative to figure 5.4.

Parameter name	Parameter	Values conf. I	Values conf. II
Half major axis length	a	178.3 mm	119.5 mm
Half minor axis length	b	124.5 mm	102.2 mm
Focal points separation	A_0	255.1 mm	123.8 mm
Focal distance horn	R_1	150.5 mm	100.7 mm
Focal distance hybrid	R_2	206.0 mm	138.2 mm
Angle of incidence	θ_i	45.00°	30.00°
See figure 5.4	θ_p	126.14°	104.82°
See figure 5.4	ψ	81.14°	74.82°
Distance to input waist	d_{in}	150 mm	100 mm
Distance to output waist	d_{out}	204.8 mm	136.3 mm
Beam width at mirror	w_m	22.4 mm	15 mm
Power in the fundamental mode	$100(P - \Delta P)$	97.54%	99.18%

parabolic mirrors with the relation $\frac{f_{\text{hybrid}}}{f_{\text{horn}}} = 1.33$ and $\frac{f_{\text{hybrid}}}{f_{\text{horn}}} = 1.40$ respectively can be found [23] and their parameters are listed in table 5.3.

An illustration on what the different mirror parameters corresponds to can be found in figure 5.5. These mirrors are not designed for use at THz frequencies but instead for use at infrared. Since the skin-depth of 500 GHz is much deeper than for infrared radiation, losses introduced due to the thickness of the reflecting surface can be present. Since no specification of surface thickness can be found, losses have to be included in the total loss found from measurements.

A rough estimation indicated that there will be no beam blockage with configuration *I* together with the horn and hybrid antenna so it was used for the final system. One mirror with Reflected focal length RFL = 101.6 mm and two with RFL = 76.2 mm was ordered. Two mirrors with RFL = 76.2 mm are used in the initial measurements to validate the quasi-optical properties of the designed measurement system.

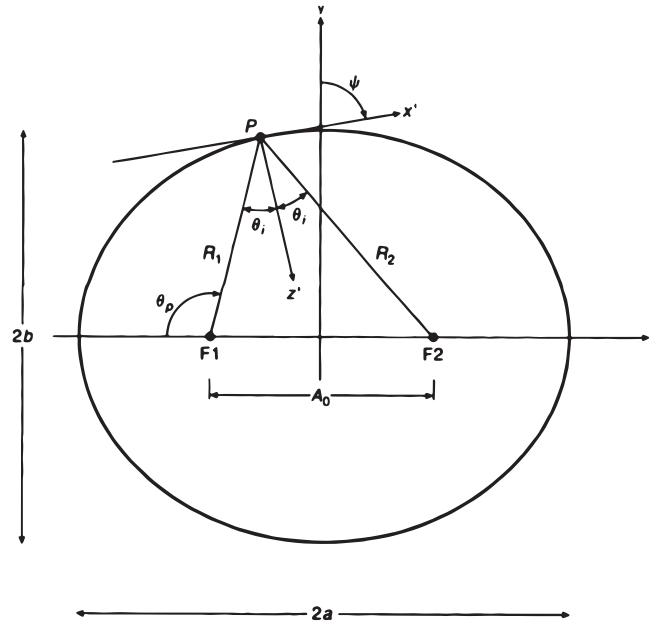


Figure 5.4: Geometry of an elliptical reflector with the two focal-points F1 and F2. The rest of the parameters can be found in table 5.2. Figure taken from [13].

Table 5.3: Parameters for two available 90° off-axis parabolic mirrors from Edmund Optics.

Parameter name	Parameter	Mirror at horn	Mirror at hybrid
Configuration I $\mathfrak{M} = 1.33$			
Reflected focal length (RFL)	f	76.2 mm	101.6 mm
Parent focal length (PFL)	f_p	38.1 mm	50.8 mm
Diameter	D	50.8 mm	50.8 mm
Thickness	T	57.2 mm	57.2 mm
F-number	$\frac{f}{D}$	1.5	2
Configuration II $\mathfrak{M} = 1.40$			
Reflected focal length (RFL)	f	127 mm	177.8 mm
Parent focal length (PFL)	f_p	63.5 mm	88.9 mm
Diameter	D	76.2 mm	76.2 mm
Thickness	T	83.8 mm	83.8 mm
F-number	$\frac{f}{D}$	$1\frac{2}{3}$	$2\frac{1}{3}$

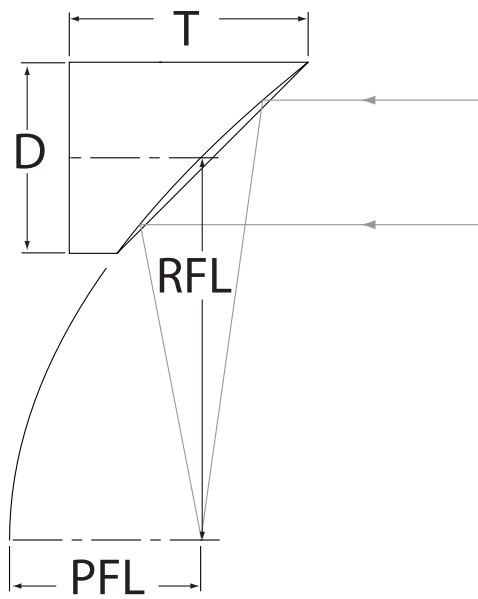


Figure 5.5: An illustration from Thorlabs [24] on what the different mirror parameters are describing.

6

Measurements and results

In this chapter the designed system will be realized and the measurements will be compared with the theoretical calculations and simulations. First an initial description of the components used and then a description of the initial calibration procedure followed by validation measurements with horns at both receiver and transmitter and finally measurements with the bolometer and the hybrid antenna.

6.1 Measurement set-up

As a RF source for all measurements, a 9.02 – 13.8 GHz YIG Oscillator with a x36 VDI TX 195 multiplier was used. This configuration gives an output frequency of 325 – 500 GHz. The radiation was coupled out to the quasi-optic waveguide through the earlier simulated diagonal horn (appendix C) via a WR-2.2 waveguide interface. The WR-2.2 waveguide specifications can be found in appendix D. For the initial testing an Erickson power meter PM2 was used as detector. The sensor of the Erickson power meter PM2 has a WR-10 waveguide interface whereas the diagonal horn has a WR-2.2 waveguide interface so a taper WR-2.2 to WR-10 was used between them. The VDI TX 195 has a WR-2.2 interface on the RF output so the horn was mounted directly to it. The source, horns, taper and power-meter are all from Virginia Diodes [11]. The sensor of the Erickson power meter and later the hybrid antenna were mounted on a ramp that could be adjusted in all three axis directions, tipped and turned horizontally. The RF source was standing on a solid Aluminium breadboard with adjustable legs and could not be finely tuned. The mirrors was mounted in 2-screw (tip and tilt) kinematic mounts on adjustable posts. A photo of the set-up in U-configuration with the hybrid antenna mount can be found in figure 6.6.

6.2 Initial calibration

To calculate the power loss in the system, the output power of the RF source must be known. The output power of the RF source was not constant over the whole specified spectrum so first the output power of certain frequencies must be found. This was done by connecting the sensor of the PM2 to the source through the taper as illustrated in figure 6.1(a).

6.2.1 Validation through waveguide taper

To simplify the initial alignment of the mirrors, source and sensor, it is desired to have the highest available output power. To find the frequency with the highest output power, the source frequency was swept over the available spectrum with the power meter connected as in figure 6.1(a). During the sweep track was kept on the output power with the power meter. The highest output power of the RF source $220 \mu\text{W}$ was measured to be at 389 GHz. This frequency was used first for the initial alignment of the mirrors and horns. Another peak of $150 \mu\text{W}$ was found at 452.5 GHz which was closer to the design frequency (500 GHz) and was used to fine-tune the set-up. The loss in the taper is about 0.5 dB [11]. However since the taper also was used between the horn and the sensor during the rest of the alignment process it was not taken in consideration now.

6.2.2 Directly horn to horn

A measurement horn to horn directly, as illustrated in figure 6.1(b) was also performed at 389 GHz. This measurement gave an output power of $152 \mu\text{W}$ which is $\frac{152}{220} \approx 0.7$ of the power that was directly coupled through the taper.

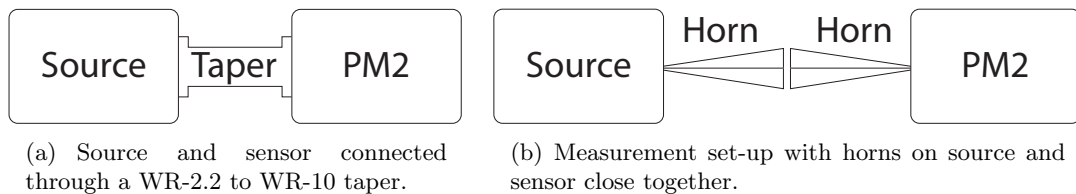


Figure 6.1: Illustrations on how the initial calibration measurements without mirrors are done. The taper from figure (a) was then connected between the sensor and horn at PM2 but is not included in figure (b).

6.2.3 Mirrors in Z-configuration

The initial measurements with mirrors were done with the mirrors in a Z-configuration as in figure 6.2(a). This was done to validate if there will be any differences as discussed earlier and described in [14] regarding the off-axis effect. Early in the calibration stage a

standing wave pattern was found in the measurement set-up. After many hours of alignment, the maximum measured power levels were found and the corresponding distances can be found in table 6.1.

Table 6.1: The maximum power levels measured with the mirrors in Z-configuration (figure 6.2(a)).

Frequency		389 GHz	452.5 GHz
Source distance from mirror	d_1	74 mm	73 mm
Sensor distance from mirror	d'_2	74 mm	75 mm
Distance between mirrors	L	18 cm	18 cm
Measured power level	P_{in}	105 μ W	84 μ W
Loss in horns and Q-O waveguide	P_{loss}	3.2 dB	2.5 dB

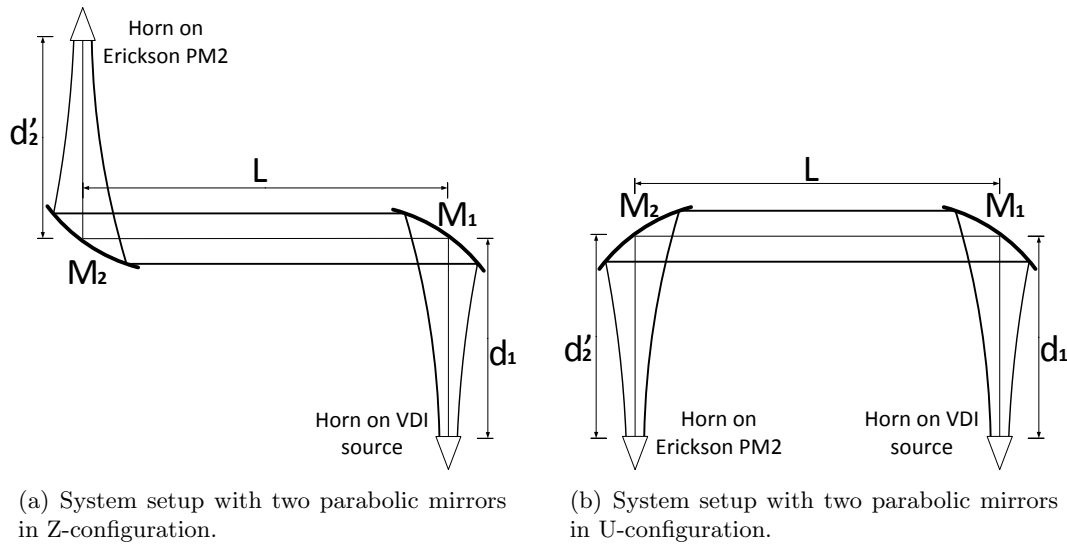


Figure 6.2: Two mirror configurations used for the measurements with the Erickson power meter. $M_{1,RFL} = M_{2,RFL} = 76.2$ mm.

6.2.4 Mirrors in U-configuration

Now the mirrors were moved and put in a U-configuration. Switching to U-configuration did not have any effect on the standing waves but the maximum measured RF power levels increased. The maximum measured power levels and the corresponding distances can be found in table 6.2 The rest of the measurements will be performed with the mirrors in a U-configuration to minimize the aberrations losses [14].

6.2.5 Standing waves

To calculate the standing wave ratio at 452.5 GHz the system was tuned in on a location with a maximum value 110 μW . Then the sensor was moved towards the mirror until the closest local minimum of 48 μW was found. These two values were then used to calculate the standing wave ratio with equation (6.1).

$$|\Gamma| = \frac{VSWR - 1}{VSWR + 1} = \frac{\sqrt{\frac{110}{48}} - 1}{\sqrt{\frac{110}{48}} + 1} \approx 0.2 \quad (6.1)$$

This gives a return loss of about 14 dB with equation (6.2)

$$RL(\text{dB}) = -20 \log |\Gamma| = -20 \log 0.2 \approx 14 \text{ dB} \quad (6.2)$$

6.2.6 Difficulties with the alignment

The alignment of the RF source and sensor relative to the mirror was found to be very critical. The standing wave pattern made the tuning harder since the equipment used was not made for such a fine tuning. Fine steps had to be used in the movement along the beam direction. Just touching the adjustment screw could result in a 20% drop in measured power. The wavelength for 452.5 GHz is approximately 0.66 mm so by just moving some component 0.17 mm along the beam direction the power dropped from a maximum to a minimum. The speed of the PM2 is also rather slow so the adjustments had to be made slowly. A maximum measured power of 111 μW was found after many hours of tuning with the source and detector at different distances and the mirrors and detector tipped and tilted in different positions and angles. The measured maximum value and the surrounding maximums can be found in figure 6.3. The green solid line is the theoretical power fitted to the maximum measured value if the beam waists have the same radius $w_0 = 1.3$ mm. Each measuring point in figure 6.3 is a local max. There are other maximums and minimums between the measuring points that are not included in the figure. The minimums level was around 50 to 60 percent below the maximums. The fact that the system induced a standing wave pattern indicates that some of the radiation was reflected. Depending on the path of the reflected wave, some of the radiation does probably not return to the detector. This was a probable factor to some of the losses that were experienced during measurements. Another factor was that the mirrors are fabricated for shorter wavelength radiation and the thickness of the reflective surface was not known so some power was probably lost due to absorption in the mirrors. Absorbing material was placed around the horns at both the source and the detector but it had no effect on the standing waves. This indicates the source of the standing waves was inside the horns and was impossible to avoid.

Since the system was designed for 500 GHz most of the effort was put on to get the best performance at the 452.5 GHz measurements which is closer to the design frequency than 389 GHz.

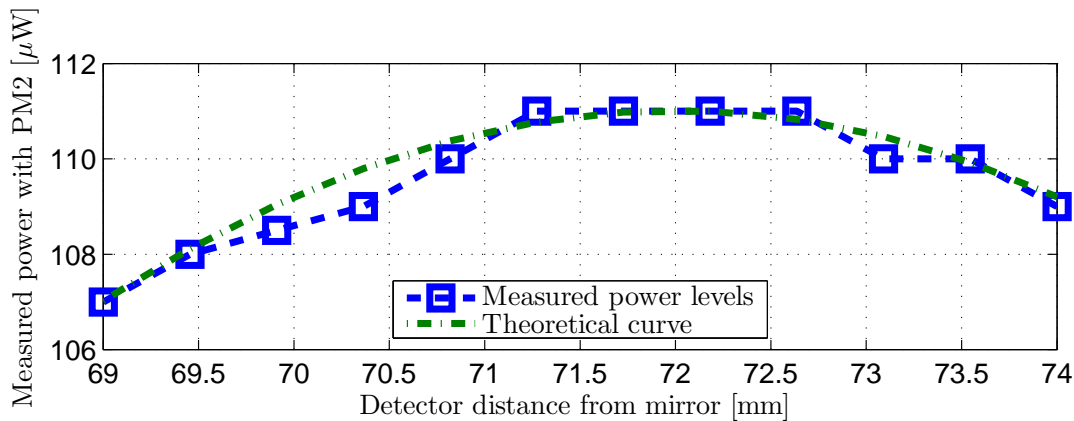


Figure 6.3: The curve with square markers were the measured powers when varying the detectors distance from second mirror and keeping source at 76 mm from first mirror and having the mirrors 18 cm apart. Curve without markers is fitted theoretical.

Table 6.2: The maximum power levels measured with the mirrors in U-configuration (figure 6.2(b)).

Frequency		389 GHz	452.5 GHz
Source distance from mirror	d_1	74 mm	73 mm
Sensor distance from mirror	d'_2	74 mm	77 mm
Distance between mirrors	L	14 cm	14 cm
Measured power level	P_{in}	154 μ W	111 μ W
Loss in horns and Q-O waveguide	P_{loss}	1.5 dB	1.3 dB

6.2.7 Removing the taper

The losses in the taper are about 0.5 dB [11]. As an experiment the taper from WR-2.2 to WR-10 was removed and the horn directly connected to the detector. This will remove the loss from the taper but give a mismatch between the horn and the WR-10 interface of the sensor. The removal of the taper gave a slightly higher measured maximum power level of 115 μ W on 452.5 GHz when the system was re-aligned after the removal. It did not have any effect on the standing waves.

6.3 Bolometer measurements

For the final tests the PM2 was replaced by a hybrid antenna with an interacted YBCO bolometer. The closest mirror was changed to the one with a reflected focal length of $M_{2,RFL} = 101.6$ mm as seen in figure 6.4. A schematic view of the measurement set-up

can be seen in figure 6.5

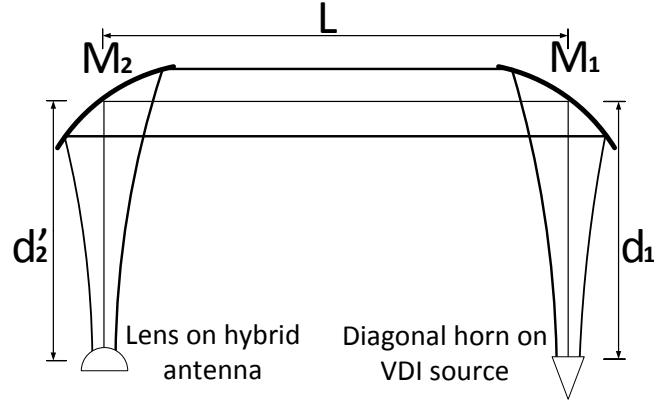


Figure 6.4: The PM2 was replaced by a hybrid antenna with bolometer and mirror M_2 was replaced by the mirror with $M_{2,RFL} = 101.6$ mm. $M_{1,RFL} = 76.2$ mm.

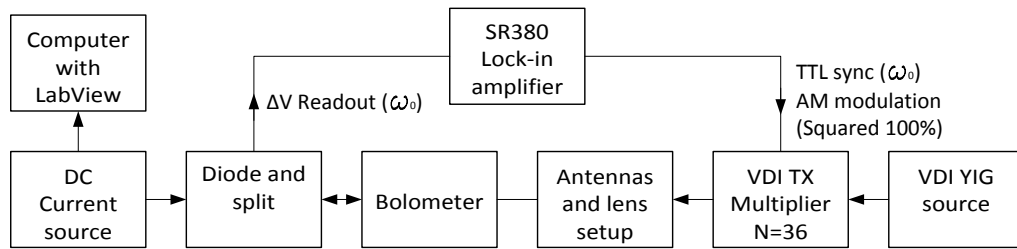


Figure 6.5: Schematic view of the measuring set-up with bolometer and hybrid antenna.

A diode was connected in parallel with the bolometer to protect the bolometer from high bias currents. Since there was no interest in finding the maximum responsivity of the bolometer in this case, the bias current was kept rather low at about 0.7 mA to minimize the risk of damaging the device. The RF source signal was amplitude modulated resulting in a voltage shift over the bolometer that was measured with a lock-in amplifier. It is clear from figure 6.7(b) that the diode kicks in above 0.7 mA and reduces the measured voltage value. The data in figure 6.7(b) was extracted by measuring the voltage rms for a fixed RF input and sweeping the bias current. The standing wave pattern was still present when measurements were done with the hybrid antenna and bolometer. Local minimums and maximums were now also found when the bolometer was tipped or tilted. This effect was due to that the sapphire substrate used for the bolometer was a uniaxial birefringent material [9] so it also made the power change depending on the incident angle. This had an effect on the alignment and the power coupling but was not be further investigated. The maximum measured voltage

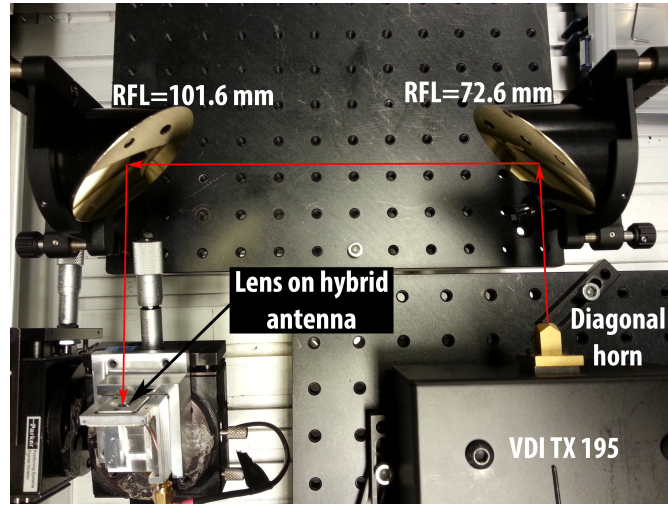
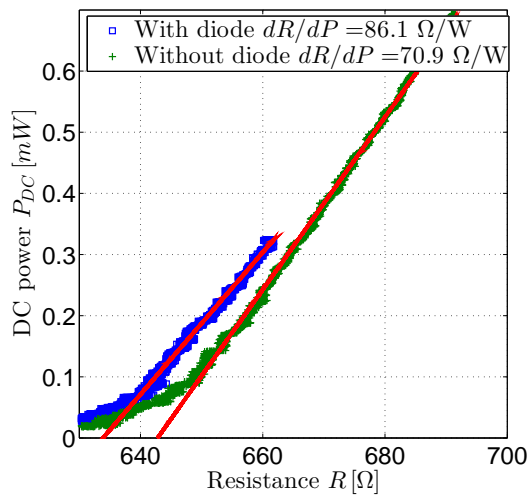
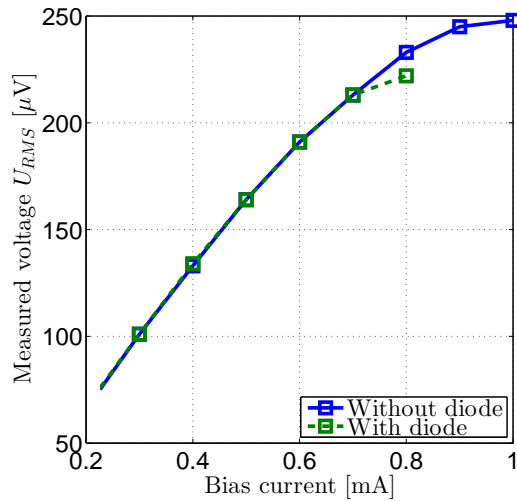


Figure 6.6: Photo of the quasi-optical waveguide set-up with the hybrid antenna mount on the left (silver) and the VDI TX 195 (black) with the diagonal horn (gold) on the right.



(a) The electrical responsivity is inversely proportional to the slope of the red line dR/dP . Higher dR/dP gives better responsivity.



(b) Bias current of the bolometer versus measured voltage rms value with and without a diode connected in parallel with the bolometer.

Figure 6.7: The responsivity is taken from the slope of the red lines in (a) multiplied with the bias current I_b . The impact of the diode can be seen in both figures.

RMS values and the corresponding parameters used for the measurement set-up can be found in table 6.3.

Table 6.3: Parameter values for maximum responsivity at measurements on the S6-6 device.

Source carrier frequency	f	389 GHz	452.5 GHz
Resistance at room temperature	$R_{300\text{K}}$	678 Ω	638 Ω
Bias current	I_b	700 μA	702 μA
Modulation frequency	f_m	664 Hz	664 Hz
Source horn distance from mirror	d_2	73 mm	73 mm
Lens distance from mirror	d'_2	106 mm	105 mm
Distance between mirrors	L	18 cm	18 cm
Measured RMS value	$U_{\text{read out}}$	436 μV	221 μV
Incident power on lens surface	P_{in}	154 μW	115 μW

6.3.1 Responsivity

To extract the data needed for the electrical responsivity calculations, the voltage over and the current through the device was measured when the bias current was swept from 0 to 0.7 mA. The electrical responsivity $S_{V,el}$ [V/W] was then calculated by plotting DC power consumption P_{DC} versus the resistance in the bolometer and then using the linear part of the curve and fitting it to a line whose gradient gives dR/dP . This was then multiplied with bias current to extract the DC responsivity. See equation (6.3).

$$\frac{dR}{dP} I_b = \frac{dU}{dP} \rightarrow \left[\frac{\Omega \times \text{mA}}{\text{mW}} \right] = \left[\frac{\text{V}}{\text{W}} \right] \quad (6.3)$$

A bias current of $I_b \approx 0.7\text{mA}$ and the data in figure 6.7(a) gave electrical responsivity of $S_{V,el} \approx 60\text{V/w}$ with the diode connected in parallel and $S_{V,el} \approx 50\text{V/w}$ without the diode in connected parallel. Why better responsivity was achieved with a diode parallel with the bolometer was probably caused by the characteristics of the used diode. Since we are close to its knee voltage it behaves like an amplifier.

From equation (2.4) we have that the optical responsivity is the ratio between voltage swing over the bolometer and the absorbed RF power $S_V = \frac{\Delta U}{\Delta P_{\text{RF}}}$. The $U_{\text{read out}}$ values from the SR380 given in table 6.3 were the RMS voltages. The total voltage swing is the peak-to-peak value $U_{\text{p-p}}$ which is two times the voltage peak value $2 \cdot U_p$ and the peak value is $U_p = \sqrt{2} \cdot U_{\text{RMS}}$. This gives $U_{\text{p-p}} = 2 \cdot \sqrt{2} \cdot U_{\text{read out}}$, giving a optical responsivity of

$$S_V = \frac{U_{\text{p-p}}}{P_{\text{RF}}} = \frac{2 \cdot \sqrt{2} \cdot U_{\text{read out}}}{P_{\text{RF}}} \quad (6.4)$$

The RF power reaching the bolometer was not the power incident on the lens surface (table 6.3). To extract the real optical responsivity of the bolometer all the losses introduced by bad coupling and mismatches needed to be taken into account. If the assumption was made that the power was the same at the hybrid antenna as in the earlier

measurement with the horns other losses still have to be considered. The polarisation mismatch from linear to elliptical polarisation was about 50% ($T_{\text{pol}} = 0.5$). The reflection loss at the surface of the lens when normal incident to the surface was assumed, give a transmission according to equation (6.5) since the index of refraction for silicon is $n \approx \sqrt{\epsilon_r} = \sqrt{11.7}$.

$$T_{\text{surf}} = 1 - R = 1 - \left| \frac{n_1 - n_2}{n_1 + n_2} \right|^2 = 1 - \left| \frac{1 - \sqrt{11.7}}{1 + \sqrt{11.7}} \right|^2 \approx 0.7 \quad (6.5)$$

Losses due to the mismatch between the bolometer and the antenna. The impedance of the bolometer is approximately $Z_L \approx 600 \Omega$ and the impedance of the antenna was assumed to be $Z_S \approx 100 \Omega$.

$$T_{\text{ant}} = 1 - \Gamma = 1 - \left| \frac{Z_L - Z_S}{Z_L + Z_S} \right|^2 = 1 - \left| \frac{600 - 100}{600 + 100} \right|^2 \approx 0.5 \quad (6.6)$$

If these losses were taken into account resulting in a total transmission coefficient of

$$T_{\text{tot}} = T_{\text{pol}} \times T_{\text{surf}} \times T_{\text{ant}} = 0.5 \times 0.7 \times 0.5 \approx 0.2 \quad (6.7)$$

This gave with equation (6.4) an optical responsivity of $S_V \approx 40 \text{ V/w}$ for the 389 GHz measurement and $S_V \approx 30 \text{ V/w}$ for the 452.5 GHz measurement.

6.3.2 Polarisation ellipse consideration

The polarisation ellipse orientation was not considered during the measurements but if the simulations are correct the origination used in the measurements should be close to the optimum according to figure 3.13(a). This since the radiation from the diagonal horn is vertically polarised and the hybrid antenna was mounted so the E-field from the diagonal horn was parallel with the Y-axis ($\varphi = 90^\circ$). As a confirmation, the hybrid antenna was also rotated $\varphi = 90^\circ$ with less power coupled to the bolometer as a result. The hybrid antenna has to be tilted as in figure 6.8(b) to get the best coupling. The reason for this was that the chip with the spiral antenna and bolometer was not perfectly centred on the backside of the lens.

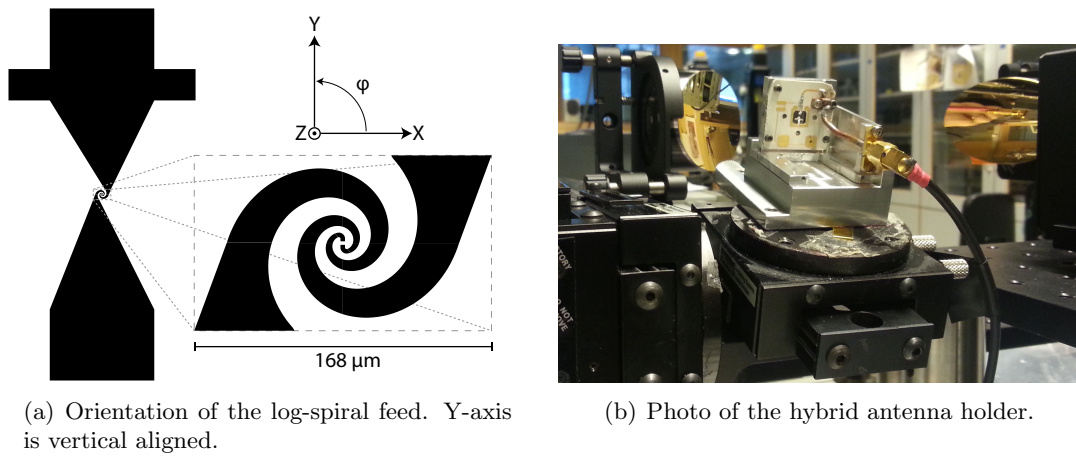


Figure 6.8: The image in figure (b) shows how the antenna is tilted upwards to get the highest optical responsivity.

7

Discussion, conclusion and future outlook

This chapter contains an overall discussion and conclusion of the thesis work. More detailed discussions and conclusions regarding the different topics and procedures can be found in their corresponding chapters.

7.1 The simulation part

The first validation simulations indicated that this method of simulating the entire hybrid antenna in CST MWS was possible with the available computer and the results were in good agreement with measurements. A lot of effort was put into finding the reason why the CST MWS side lobe pattern (figure 3.4) was so different compared with the Jellema et al. publication [18]. The conclusion was drawn that this was due to external factors that were not included in the simulation. The largest uncertainty from the CST MWS simulation part was the phase centre position. When a lens was involved the standard deviation σ was always too large to give any consistency in the results. The reason for this is still unclear. Simulations indicated that the size of the log-spiral feed was not optimal for the low frequencies used during the measurements. Fabrications of bolometers with larger log-spiral feed are already in process but measurements on those devices will not be included in this thesis. The nonphysical results from the Agilent ADS momentum simulations were probably caused by a bug in the software. Some bugs that can be related to this problem has been announced by Agilent and will probably be corrected in the next version of the software.

7.2 Quasi-optical waveguide

The standing waves in the quasi-optical waveguide were a problem during the alignment process. For the high frequencies used during the measurements it would be preferable to have more precise alignment possibilities. With the available equipment the alignment was very time consuming. But since the same maximum value was found for different positions of source and detector the conclusion is drawn that minimum loss of 1.3 dB for 452.5 GHz was close to the physical minimum for the quasi-optical waveguide. The fundamental Gaussian mode content for the diagonal horn is specified to be 84%. So the fundamental Gaussian mode coupling between the diagonal horns is 0.7 since $0.84 \cdot 0.84 \approx 0.7$ which corresponds to 1.5 dB in loss.

7.3 Bolometer measurements

The resistance of the bolometer changed with time as seen in appendix B. The bolometer chip was stored in a nitrogen environment but as soon as it was used in the oxygen rich air, the oxygen deteriorated the device so it would eventually become unusable. If figure 6.7(a) is compared with appendix B it is obvious that the measurements for figure 6.7(a) were done after the measurements in the appendix since the resistance was higher. In the calculation of the transmission coefficient rough estimations were done so consequently the accuracy on the calculated optical responsivity was very uncertain.

7.4 Future outlook

Since this thesis include several different topics, more work can be put in to all of them. Here are some suggestions:

- It was mentioned in section 3.1.2 that with CST MWS 2013 it is possible to simulate with higher number of mesh cells than in the earlier version which was mostly used in the thesis. With the newer version the hybrid antenna could then be simulated for higher frequencies and then also use the supported multi-core GPU possibility to speed up the calculations.
- It would be interesting to simulate the entire quasi-optical waveguide in GRASP or similar software and compare the results with the measurements and calculations in the thesis. Simulations can then be done with higher modes included and not just the fundamental Gaussian mode to get more accurate results.
- The transmission coefficient calculations can be further investigated. Then the birefringence of the sapphire substrate would have to be more investigated and also the impedance of the antenna which was assumed to be 100Ω in the calculations.

References

- [1] F. Sizov, “Thz radiation sensors,” *Opto-electronics review*, vol. 18, no. 1, pp. 10–36, 2010.
- [2] P. H. Siegel, “Terahertz technology,” *Microwave Theory and Techniques, IEEE Transactions on*, vol. 50, no. 3, pp. 910–928, 2002.
- [3] J. Federici and L. Moeller, “Review of terahertz and subterahertz wireless communications,” *Journal of Applied Physics*, vol. 107, no. 11, pp. 111 101–111 101, 2010.
- [4] S. Cherednichenko, A. Hammar, S. Bevilacqua, V. Drakinskiy, J. Stake, and A. Kalabukhov, “A room temperature bolometer for terahertz coherent and incoherent detection,” *Terahertz Science and Technology, IEEE Transactions on*, vol. 1, no. 2, pp. 395–402, nov. 2011.
- [5] S. P. Langley, “The bolometer and radiant energy,” *Proceedings of the American Academy of Arts and Sciences*, vol. 16, pp. pp. 342–358, 1880. [Online]. Available: <http://www.jstor.org/stable/25138616>
- [6] P. Richards, “Bolometers for infrared and millimeter waves,” *Journal of Applied Physics*, vol. 76, no. 1, pp. 1–24, 1994.
- [7] K. A. Müller and J. G. Bednorz, “The discovery of a class of high-temperature superconductors,” *Science*, vol. 237, no. 4819, pp. pp. 1133–1139, 1987. [Online]. Available: <http://www.jstor.org/stable/1699508>
- [8] D. F. Filipovic, S. S. Gearhart, and G. M. Rebeiz, “Double-slot antennas on extended hemispherical and elliptical silicon dielectric lenses,” *Microwave Theory and Techniques, IEEE Transactions on*, vol. 41, no. 10, pp. 1738–1749, 1993.
- [9] E. D. Palik, *Handbook of Optical Constants of Solids: Index*. Access Online via Elsevier, 1998, vol. 3.
- [10] A. Semenov, H. Richter, H.-W. Hubers, B. Gunther, A. Smirnov, K. Il’in, M. Siegel, and J. Karamarkovic, “Terahertz performance of integrated lens antennas with a

- hot-electron bolometer,” *Microwave Theory and Techniques, IEEE Transactions on*, vol. 55, no. 2, pp. 239–247, 2007.
- [11] “Virginia Diodes homepage,” 2013. [Online]. Available: <http://vadiodes.com/>
- [12] C. A. Balanis, *Antenna Theory: Analysis and Design*. Wiley-Interscience, 2005.
- [13] P. F. Goldsmith *et al.*, *Quasioptical systems*. Chapman & Hall, 1998.
- [14] J. Murphy, “Distortion of a simple gaussian beam on reflection from off-axis ellipsoidal mirrors,” *International journal of infrared and millimeter waves*, vol. 8, no. 9, pp. 1165–1187, 1987.
- [15] P. Belland and J. P. Crenn, “Changes in the characteristics of a gaussian beam weakly diffracted by a circular aperture,” *Appl. Opt.*, vol. 21, no. 3, pp. 522–527, Feb 1982. [Online]. Available: <http://ao.osa.org/abstract.cfm?URI=ao-21-3-522>
- [16] “CST - Computer Simulation Technology homepage,” 2013. [Online]. Available: <http://www.cst.com/>
- [17] M. J. van der Vorst, P. J. de Maagt, A. Neto, A. L. Reynolds, R. M. Heeres, W. Luinge, and M. H. Herben, “Effect of internal reflections on the radiation properties and input impedance of integrated lens antennas-comparison between theory and measurements,” *Microwave Theory and Techniques, IEEE Transactions on*, vol. 49, no. 6, pp. 1118–1125, 2001.
- [18] W. Jellema, T. J. Finn, A. Baryshev, M. van der Vorst, S. Withington, J. A. Murphy, and W. Wild, “Phase-Sensitive Near-Field Measurements and Electromagnetic Simulations of a Double-Slot HEB Integrated Lens-Antenna Mixer at 1.1, 1.2 and 1.6 THz,” in *Sixteenth International Symposium on Space Terahertz Technology*, May 2005, pp. 398–403.
- [19] “Agilent homepage,” 2013. [Online]. Available: <http://www.home.agilent.com/en/pc-1297113/advanced-design-system-ads>
- [20] “MathWorks homepage,” 2013. [Online]. Available: <http://www.mathworks.com/>
- [21] C. Brückner, G. Notni, and A. Tünnermann, “Optimal arrangement of 90 off-axis parabolic mirrors in thz setups,” *Optik-International Journal for Light and Electron Optics*, vol. 121, no. 1, pp. 113–119, 2010.
- [22] S. Withington, J. Murphy, and K. Isaak, “Representation of mirrors in beam waveguides as inclined phase-transforming surfaces,” *Infrared physics & technology*, vol. 36, no. 3, pp. 723–734, 1995.
- [23] “Edmund Optics Ltd homepage,” 2013. [Online]. Available: <http://www.edmundoptics.com/>
- [24] “Thorlabs homepage,” 2013. [Online]. Available: <http://www.thorlabs.com/>

A

Additional far-fields comparisons

Figure A.1 shows additional comparisons with the Van der Vorst paper et al. publication [17]. CST MWS was used for the simulations. All simulations were done at 497 GHz with the same specification as in table 3.1. The reason for the large differences in the H-plane for the $\varnothing = 4$ mm lens with no anti reflection coating was not further investigated.

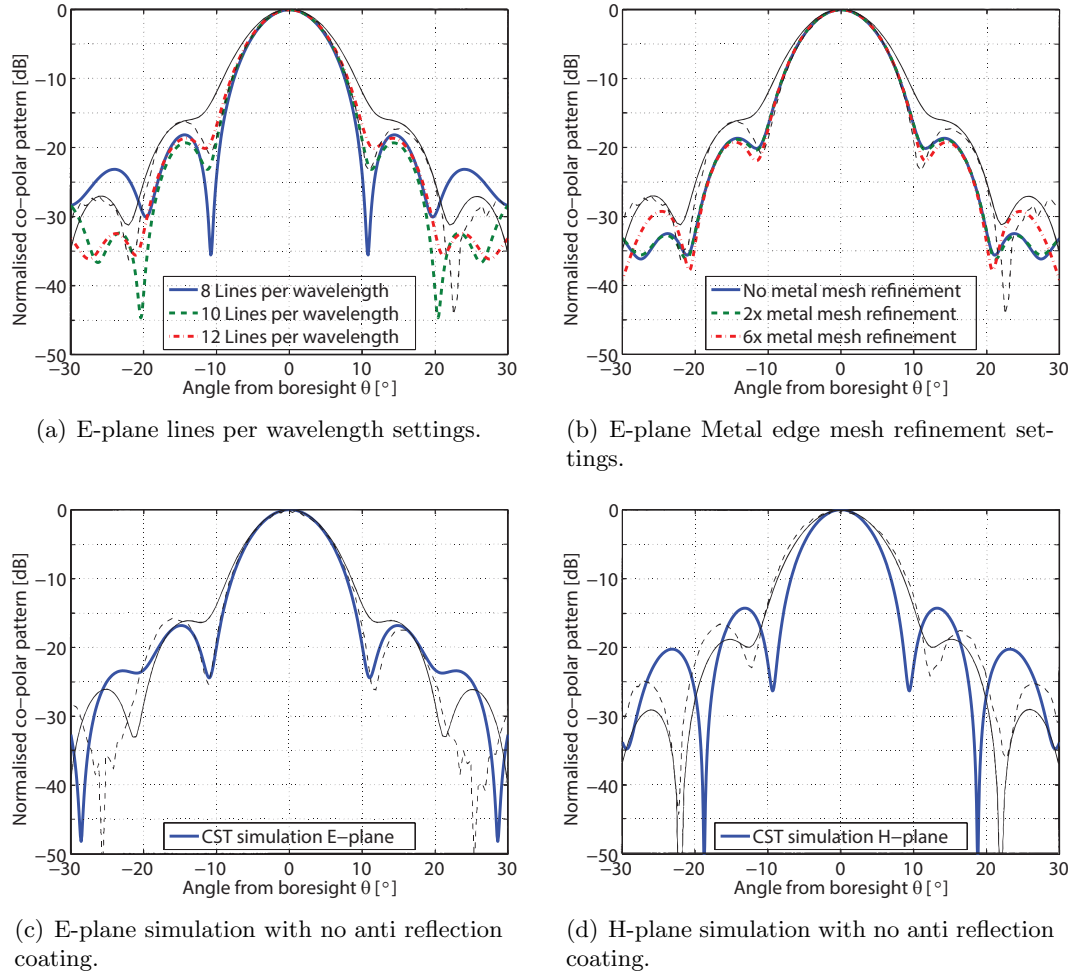


Figure A.1: Additional comparisons with Van der Vorst paper et al. publication [17]. The black thin lines are the simulated (—) and measured (- -) results from the publication.

B

Deterioration of bolometer

The bolometer devices are usually stored in a nitrogen environment to retain their properties. Figure B.1 shows the change of the bolometers characteristics when exposed to the atmosphere.

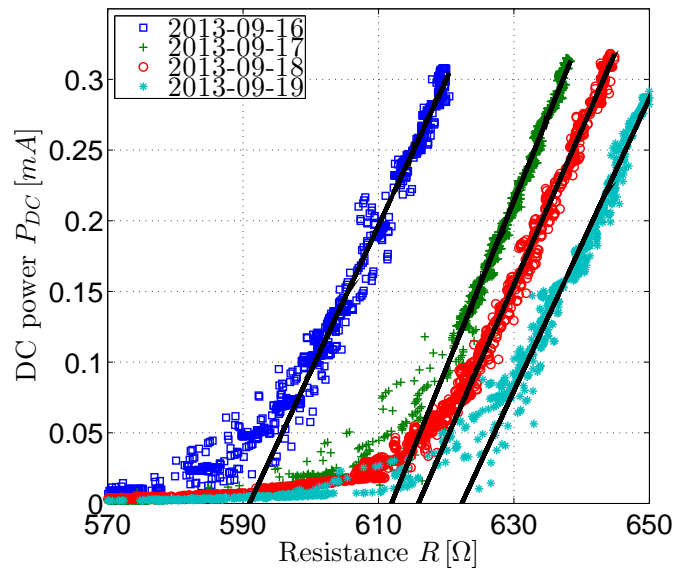


Figure B.1: The change of the resistance over time is clearly seen in the figure. The responsivity is calculated from the fitted lines in the figure.

C

VDI nominal horn specifications

Nominal Horn Specifications

10/31/11

Waveguide Band	Freq. Range (GHz)	Horn Type	Physical Parameters			Electrical Parameters (calculated at mid-Band)		
			Horn Length (mm)	Aperture Diameter (mm)	Taper Half-Angle (deg)	Full 3 dB Beamwidth (deg)	Gain (dB)	Beam Waist Radius (mm)
WR-10	75 - 110	Conical	35.5	16.3	12.9	13	21	6.2
WR-8	90 - 140	Conical	35.5	13.6	10.8	12	21	5.2
WR-6.5	110 - 170	Conical	26.0	10.8	11.7	13	21	4.1
WR-5.1	140 - 220	Conical	20.5	8.4	11.6	13	21	3.2
WR-4.3	170 - 260	Conical	16.5	7.1	12.1	13	21	2.7
WR-3.4	220 - 325	Diagonal	26.4	5.6	6.0	12	25	2.0
WR-2.8	260 - 400	Diagonal	21.4	4.6	6.1	12	25	1.7
WR-2.2	325 - 500	Diagonal	16.8	3.6	6.1	12	25	1.3
WR-1.9	400 - 600	Diagonal	15.4	3.1	5.7	11	25	1.1
WR-1.5	500 - 750	Diagonal	11.8	2.4	5.8	12	25	0.89
WR-1.2	600 - 900	Diagonal	10.7	2.0	5.3	11	25	0.76
WR-1.0	750 - 1100	Diagonal	9.0	1.6	5.2	11	25	0.62
WR-0.8	900 - 1400	Diagonal	6.8	1.3	5.5	11	25	0.49
WR-0.65	1100 - 1700	Diagonal	5.9	1.06	5.1	11	25	0.41
WR-0.51	1400 - 2200	Diagonal	4.6	0.84	5.2	11	25	0.32
WR-0.4	1800 - 2800	Diagonal	3.6	0.65	5.2	11	25	0.25
WR-0.34	2200 - 3250	Diagonal	3.1	0.56	5.2	11	25	0.21

Beamwidth and Radius are averages of E- and H-plane patterns

Fundamental Gaussian Mode Content

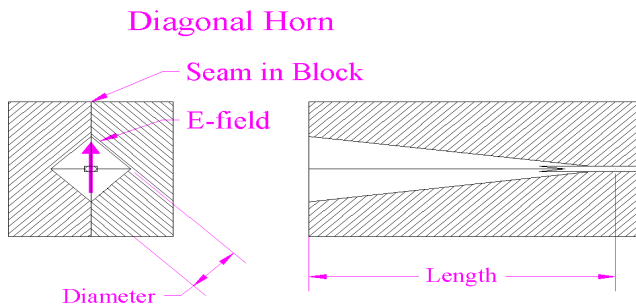
- 87% typical for Conical Horn
- 84% typical for Diagonal Horn

References

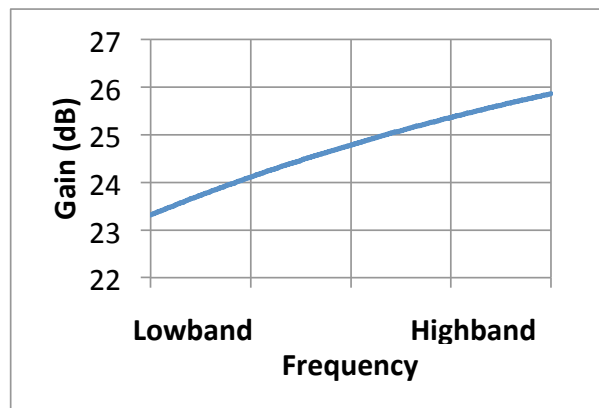
- Quasioptical Systems, Paul Goldsmith, IEEE Press, 1998
- The Handbook of Antenna Design Vol. 1, A.W. Rudge et al. (ed.), IEE Press, 1982
- Microwave Horns and Feeds, Olver, A.D., et al., IEE Electromagnetic Waves Series. 39
- Microwave Engineering & Applications, Gandhi, Om P., Pergamon Press, 1981
- "The Diagonal Horn as a Sub-Millimeter Wave Antenna," Johansson et al, IEEE-MTT40, May 1992, pp. 795-800

Aperture Diameter for Diagonal Horn

Taper angle measured from center line to nearest horn wall



Typical Gain vs Frequency



D

VDI waveguide band designations

Virginia Diodes Inc. Waveguide Band Designations

Last Modified : 6/29/2010



Internal Band Designation	EIA Band Designation	Internal Dimensions (mils)	Internal Dimensions (mm)	Frequency Range (GHz)	TE(10) Cutoff (GHz)	WG Loss Low - High ¹ (dB/mm)	Flange Designation	Description	Letter Desig.
WR- 51.0	WR- 51	510 x 255	12.954 x 6.477	15.0 - 22.0	11.6	0.0005 - 0.0004			
WR- 42.0	WR- 42	420 x 170	10.668 x 4.318	17.5 - 26.5	14.0	0.0008 - 0.0006			K
WR- 34.0	WR- 34	340 x 170	8.636 x 4.318	22.0 - 33.0	17.4	0.001 - 0.0007			
WR- 28.0	WR- 28	280 x 140	7.112 x 3.556	26.5 - 40.0	21.1	0.0013 - 0.0009	UG-599/U	Square, Four hole fixing	Ka
WR- 22.4	WR- 22	224 x 112	5.690 x 2.845	33.0 - 50.5	26.3	0.0019 - 0.0013	UG-383/U	Circular, Four hole fixing/doweled	Q
WR- 18.8	WR- 19	188 x 94	4.775 x 2.388	40.0 - 60.0	31.4	0.0023 - 0.0016	UG-383/UM	Circular, Four hole fixing/doweled	U
WR- 14.8	WR- 15	148 x 74	3.759 x 1.880	50.5 - 75.0	39.9	0.0034 - 0.0024	UG-385/U	Circular, Four hole fixing/doweled	V
WR- 12.2	WR- 12	122 x 61	3.099 x 1.549	60.0 - 90.0	48.4	0.0047 - 0.0032	UG-387/U	Circular, Four hole fixing/doweled	E
WR- 10.0	WR- 10	100 x 50	2.540 x 1.270	75.0 - 110.0	59.0	0.0061 - 0.0043	UG-387/UM	Circular, Four hole fixing/doweled	W
WR- 8.0	WR- 8	80 x 40	2.032 x 1.016	90.0 - 140.0	73.8	0.0092 - 0.0059	UG-387/UM	Circular, Four hole fixing/doweled	F
WR- 6.5	WR- 6	65 x 32.5	1.651 x 0.826	110.0 - 170.0	90.8	0.0128 - 0.0081	UG-387/UM	Circular, Four hole fixing/doweled	D
WR- 5.1	WR- 5	51 x 25.5	1.295 x 0.648	140.0 - 220.0	116	0.0185 - 0.0117	UG-387/UM	Circular, Four hole fixing/doweled	G
WR- 4.3	WR- 4	43 x 21.5	1.092 x 0.546	170.0 - 260.0	137	0.0227 - 0.0151	UG-387/UM	Circular, Four hole fixing/doweled	
WR- 3.4	WR- 3	34 x 17	0.864 x 0.432	220.0 - 330.0	174	0.0308 - 0.0214	UG-387/UM	Circular, Four hole fixing/doweled	
WR- 2.8	n/a	28 x 14	0.711 x 0.356	260.0 - 400.0	211	0.0436 - 0.0287	UG-387/UM	Circular, Four hole fixing/doweled	
WR- 2.2	n/a	22 x 11	0.559 x 0.279	330.0 - 500.0	268	0.063 - 0.041	UG-387/UM	Circular, Four hole fixing/doweled	
WR- 1.9	n/a	19 x 9.5	0.483 x 0.241	400.0 - 600.0	311	0.072 - 0.051	UG-387/UM	Circular, Four hole fixing/doweled	
WR- 1.5	n/a	15 x 7.5	0.381 x 0.191	500.0 - 750.0	393	0.105 - 0.073	UG-387/UM	Circular, Four hole fixing/doweled	
WR- 1.2	n/a	12 x 6	0.305 x 0.152	600.0 - 900.0	492	0.159 - 0.104	UG-387/UM	Circular, Four hole fixing/doweled	
WR- 1.0	n/a	10 x 5	0.254 x 0.127	750.0 - 1100.0	590	0.192 - 0.135	n/a		
WR- 0.8	n/a	8 x 4	0.203 x 0.102	900.0 - 1400.0	738	0.292 - 0.188	n/a		
WR- 0.65	n/a	6.5 x 3.25	0.165 x 0.083	1100.0 - 1700.0	908	0.406 - 0.258	n/a		
WR- 0.51	n/a	5.1 x 2.55	0.130 x 0.065	1400.0 - 2200.0	1157	0.586 - 0.369	n/a		

1) The waveguide loss is calculated assuming the conductivity of Gold, and a surface roughness factor of 1.5. The two values listed represent the loss at the low end and high end of the frequency range.